Geochimica et Cosmochimica Acta 361 (2023) 40–66

Contents lists available at ScienceDirect

Geochimica et Cosmochimica Acta

journal homepage: www.elsevier.com/locate/gca

Kinetic partitioning of trace cations between zoned clinopyroxene and a variably cooled-decompressed alkali basalt: Thermodynamic considerations on lattice strain and electrostatic energies of substitution

Silvio Mollo [a,b,*], Piergiorgio Moschini [a], Teresa Ubide [c], Alice MacDonald [c], Francesco Vetere [d], Manuela Nazzari [b], Valeria Misiti [b], Nobuyoshi Miyajima [e], Caterina Melai [e], Danilo Di Genova [f], Alessandro Vona [g], Fabrizio Di Fiore [g], Claudia Romano [g]

[a] Department of Earth Sciences, Sapienza – University of Rome, P. le Aldo Moro 5, 00185 Roma, Italy
[b] National Institute of Geophysics and Volcanology, Section of Roma 1, Via di Vigna Murata 605, 00143 Roma, Italy
[c] School of Earth and Environmental Sciences, The University of Queensland, St Lucia, 4072 Brisbane, QLD, Australia
[d] Department of Physical Sciences, Earth and Environment, University of Siena, Italy
[e] Bayerisches Geoinstitut, University of Bayreuth, Bayreuth 95440, Germany
[f] Institute of Environmental Geology and Geoengineering, National Research Council of Italy, Rome, Italy
[g] Dipartimento di Scienze, University of Roma Tre, L.go San Leonardo Murialdo 1, 00146 Roma, Italy

ARTICLE INFO

Associate editor: Rajdeep Dasgupta

Keywords:
Kinetic partitioning
Cooling and decompression
Clinopyroxene sector zoning, concentric zoning, and patchy zoning
Lattice strain and electrostatic energies of cation substitutions

ABSTRACT

We present kinetic partitioning data for trace cations measured in zoned clinopyroxene crystals obtained from a variably cooled and decompressed olivine basalt erupted at Mt. Etna volcano in Italy. Supersaturation effects and compositional heterogeneities at the interface melt lead to the development of sector zoning, concentric zoning, and patchy zoning in clinopyroxene crystals. Apparent partition coefficients between compositionally different growth layers and adjacent melts (D_i) for isovalent groups of trace elements are tested for internal consistency on the thermodynamic basis of lattice strain (ΔG_{strain}) and electrostatic (ΔG_{elec}) energies of substitutions. The excess energy of partitioning ($\Delta G_{partitioning}$) for trace cations in zoned crystals accounts for a kinetic incorporation control leading to large enthalpic effects through distortion of the lattice and changes in the electrostatic forces. $\Delta G_{partitioning}$ depends upon the complementary relationship between ΔG_{strain} and ΔG_{elec}, which is the most appropriate thermodynamic description for the accommodation of rare earth elements and high field strength elements in the lattice site of zoned crystals. Polyhedral sectors, skeletal forms, and overgrowth zones have D_i values settled by the number of charge-balanced and -imbalanced configurations taking place in the lattice site as a function of aluminium in tetrahedral coordination, and crystal structural changes produced by heterovalent cation substitutions. In an energetically unstable macroscopic system ruled by cooling and decompression, thermodynamic requirements for the crystallochemical control of D_i encompass the attainment of local equilibrium at the crystal-melt interface via the establishment of small-volume reaction kinetics. The requisite of local interface equilibrium is however susceptible to the anisotropic growth velocity of each specific clinopyroxene surface, thereby giving reason to different energetic properties of the crystallographic site. This axiomatic control requires that transition metal cations partition also in consideration of electronic effects related to the crystal field stabilization energy. The overriding implication is that D_i values for trace cations having different size, charge, and electronic configuration serve as sensitive probes of the different crystal growth mechanisms, surface incorporation sites, and arrangements of atoms at the lattice-scale. In this perspective, fractional crystallization modeling of 2011–2013 bulk rock data from lava fountains indicates that the compositional evolution of magmas erupted at Mt. Etna cannot be described by a unique equilibrium value of D_i for a given clinopyroxene-melt interface. The leverage of interface kinetics is distinctively dominant along the subvolcanic plumbing system, thereby requiring that values of D_i differ for structurally and compositionally distinct zones in clinopyroxene phenocrysts. To successfully interpret the trace element signature of Etnean magmas, the archetypal constancy of

* Corresponding author at: Department of Earth Sciences, Sapienza – University of Rome, P. le Aldo Moro 5, 00185 Roma, Italy.
E-mail address: silvio.mollo@uniroma1.it (S. Mollo).

https://doi.org/10.1016/j.gca.2023.10.012
Received 25 April 2023; Accepted 6 October 2023
Available online 9 October 2023
0016-7037/© 2023 The Author(s). Published by Elsevier Ltd. This is an open access article under the CC BY license (http://creativecommons.org/licenses/by/4.0/).

partition coefficient at bulk thermodynamic equilibrium must be in some measure reappraised in favor of the establishment of a local interface equilibrium upon highly dynamic crystallization and growth conditions.

1. Introduction

Variable cooling, decompression, and degassing mechanisms control the textual and compositional evolutions of clinopyroxene phenocrysts in volcanic rocks. In spite of these dynamic crystallization conditions, the kinetic partitioning of trace cations and their incorporation mechanisms in compositionally zoned clinopyroxene crystals have been the focus of a restricted range of experimental studies (Kouchi et al., 1983; Adam and Green, 1994; McKay et al., 1994; Lofgren et al., 2006; Mollo et al., 2013; Bonechi et al., 2021; Di Fiore et al., 2021; MacDonald et al., 2022). These studies have highlighted a strong crystallochemical control on the accommodation of trace cations in the different crystal zones when growth kinetics preclude uniform equilibrium crystallization. The main reason for such partitioning behavior is that the distribution of cations between the M1 (octahedral)- and M2 (eight-fold)-sites of clinopyroxene is highly ordered (Adam and Green, 1994) and under conditions of moderate to rapid growth, elemental partitioning is dominated by the intrinsic properties of a single crystallographic site in relation to the optimum cation radius and charge for that specific site. This principle is complemented and balanced by the entry of highly charged trace cations in clinopyroxene via substitution reactions driven by changes in the major-element crystal composition (most notably, aluminium substituting for silicon in the tetrahedral site; McKay et al., 1994; Mollo et al., 2013; MacDonald et al., 2022). Furthermore, rapid crystal growth rates imposed by extremely fast cooling conditions (i.e., 100–1000 °C/h; Lofgren et al., 2006) or, alternatively, convective mass transport in physically perturbed systems (i.e., melt stirring at shear rates of 1–10 s^{-1}; Di Fiore et al., 2021) may overwhelm the crystallographic control on trace cation partitioning and lead to deviation from regular relationships between cation size and partition coefficient.

The purpose of this work is to understand the most important mechanisms governing the incorporation of trace cations into the lattice site of clinopyroxene in response to the kinetics and energetics of crystallization typically encountered at subvolcanic conditions. The phenomenological aspects related to the partitioning of trace cations between zoned clinopyroxene and an alkaline olivine basalt melt cooled and decompressed at different rates are experimentally examined, with the final scope to reproduce the composite growth history documented for natural phenocrysts at Mt. Etna, Italy. This is a noteworthy example of open-conduit volcano characterized by a feeding system persistently filled with mafic alkaline magmas that migrate upwards through interconnected polybaric-polythermal reservoirs and vigorously mix prior to eruption at the surface (Ubide and Kamber, 2018; Ubide et al., 2019a; Moschini et al., 2021). Clinopyroxene phenocrysts show strong evidence of complex zoning patterns that may individually or mutually develop as concentric, sector, and overgrowth zones in response to the effect of highly dynamic conditions and reaction kinetics far from bulk thermodynamic equilibrium (Downes, 1974; Duncan and Preston, 1980; Ubide and Kamber, 2018; Ubide et al., 2019a; Mollo et al., 2015, 2020a).

Apparent partition coefficients presented here are intrinsically related to the kinetic aspects of crystal growth and thermodynamic mixing properties of $CaMgSi_2O_6$ and $CaAl_2SiO_6$ end-member components. The appropriate criterion for the description of trace cation partitioning requires knowledge of the complementary effects of lattice strain (ΔG_{strain}) and electrostatic (ΔG_{elec}) energies of substitutions (Blundy and Wood, 1994, 2003; Wood and Blundy, 1997, 2001). The excess energy change ($\Delta G_{partitioning}$) involved in the accommodation of a trace cation with ionic radius and/or charge different from those of the cation originally hosted in the lattice site can be expressed through the same thermodynamic principles observed under equilibrium crystallization conditions: $\Delta G_{partitioning} = \Delta G_{strain} + \Delta G_{elec}$ (Wood and Blundy, 2001). In this perspective, the partitioning of trace cations in structurally and compositionally different clinopyroxene zones is locally governed by the number of charge-balanced and -imbalanced configurations that are not compensated by full aluminium occupancy in tetrahedral coordination. The validity of this substitution mechanism is however mediated by the growth velocity of a given crystalline layer and crystal field effects arising from the electronic structure of cations. Finally, it is proposed that a set of apparent partition coefficients may serve as a suitable proxy for modeling fractional crystallization of magmas ascending along the highly dynamic plumbing system of Mt. Etna.

2. Methods

2.1. Cooling and decompression experiments

The synthetic starting material used for the experiments reproduces the composition of an alkali olivine basalt from a volcanic neck cropping out in proximity to the Paternò town (SW foot of Mt. Etna in Italy; Tanguy, 1978; Joron and Treuil, 1984; Tanguy et al., 1997; Armienti et al., 2007), dated at ~217,000 BP (Condomines et al., 1982). This is the most primitive sample erupted during the early magmatic stage of Mt. Etna and is considered transitional between tholeiitic and alkaline (Tanguy, 1978; Tanguy et al., 1997). According to Kamenetsky and Clocchiatti (1996), tholeiitic and alkaline successions reflect multistage melting and subsequent metasomatism of an upper mantle peridotite, causing systematic transitions in age, mineralogy, and geochemistry of erupted products. Mantle depletion in the basaltic component results from melt extraction with contemporaneous formation of metasomatic zones due to reaction with percolating fluids/melts. This causes the temporal shift in Etnean compositions towards alkali basalt with increasing involvement of the enriched component in magma generation (Kamenetsky and Clocchiatti, 1996).

The starting glass was synthesized at the HP-HT Laboratory of Experimental Volcanology and Geophysics of the Istituto Nazionale di Geofisica e Vulcanologia (INGV) in Rome (Italy) from a mixture (~10 g) of analytical grade SiO_2, TiO_2, $Al(OH)_3$, Fe_2O_3, MnO, $Mg(OH)_2$, $CaCO_3$, Na_2CO_3, K_2CO_3, and P_2O_5. An Fe-presaturated Pt-crucible with the starting mixture was loaded into a 1 atm vertical tube of CO–CO_2 gas-mixing furnace imposing an oxygen fugacity of 2 log units above the Ni-NiO buffer. The temperature was increased to 1100 °C in 12 h and held constant for further 12 h to attain decarbonation of the mixture. To achieve trace element contents analyzable with a high precision, the powdered material was subsequently doped with additional oxides representative of the most important geochemical groups for rare earth elements (0.5 wt% REE), high field strength elements (0.5 wt% HFSE), large ion lithophile elements (1.5 wt% LILE) and transition elements (0.5 wt% TE). Obeyance of Henry's Law was guarantee using a maximum doping level for trace element oxides not exceeding 3 wt%. According to experiments carried out at varying doping levels by Green and Pearson (1985) and Beattie (1993), the partition coefficient between clinopyroxene and melt is always independent of the concentration for trace element oxides in the bulk composition up to 4 wt%. It must be noted, however, that Henry's Law is obeyed at concentrations from ppm to the wt.% levels only in the case of homovalent cation substitutions, where the crystallochemical control on trace element partitioning is a function of radius and charge (Wood and Blundy, 2014). In contrast, heterovalent cation substitutions require local excess charge in the crystal structure, with consequent violation of Henry's law and profound dependence of trace element partitioning on the concentrations of other atoms (Wood and Blundy, 2014). After a superliquidus

treatment at 1300 °C for 2 h in order to obtain a melt homogenization, the glass was quenched in deionized water, removed from the Pt-crucible, and crushed into a fine powder. No element volatilization is expected during superliquidus treatment because gas–melt interface devolatilization reactions are hampered by the slow diffusivity of most of the trace elements added to the starting material (Zhang, 2010). Microprobe analyses performed on glass chips extracted from the top, middle, and bottom of the Pt-crucible demonstrated homogeneity and the absence of crystalline phases (Table S1).

The crystallization experiments were carried out with an internally heated pressure vessel (IHPV) at the Institute for Mineralogy, Leibniz University of Hannover (Germany). The powdered starting material was loaded into Fe-presaturated Pt capsules (inner diameter and length of 2.7 and 20 mm, respectively) containing H_2O in excess ($P_{tot} = P_{H2O}$) added as deionized water for both isobaric (400 MPa) and decompression (from 400 to 100 MPa) experiments (Table 1). The selected pressure range of 100–400 MPa matches with typical magma storage at shallow (~3 km) and mid-crustal (~12 km) reservoirs at Mt. Etna volcano (cf. Ubide and Kamber, 2018 and references therein). Comparative calculations based on the Gibbs free energy minimization algorithm (rhyolite-MELTS v.1.2.0) developed by Gualda et al. (2012) and the equation of state proposed by Duan (2014) were used to quantify the amount of water dissolved in the melt ($H_2O_{dissolved}$), the melt's liquidus temperature ($T_{liquidus}$), and the saturation temperature of clinopyroxene (T_{cpx}). Results indicate that $H_2O_{dissolved} = 3.1$ wt%, $T_{liquidus} = 1{,}116$ °C, and $T_{cpx} = 1{,}093$ °C at 100 MPa, whereas $H_2O_{dissolved} = 7.6$ wt%, $T_{liquidus} = 1{,}091$ °C, and $T_{cpx} = 1{,}068$ °C at 400 MPa (Table 1). The isobaric experiment carried out at 400 MPa ($\Delta P/\Delta t = 0$ MPa/s) is herein defined as *EXP-0*, while *EXP-0.01* and *EXP-1* refer to experiments decompressed from 400 to 100 MPa at slow ($DR_{slow} = 0.01$ MPa/s) and fast ($DR_{fast} = 1$ MPa/s) rates (Table 1). Assuming a lithostatic pressure gradient of ~0.3 MPa/m (cf. Nazzari et al., 2019), DR_{slow} and DR_{fast} corresponds to the slow (~0.03 m/s) and fast (~3.3 m/s) ascent velocities of magmas erupted at Mt. Etna (Aloisi et al., 2006; Armienti et al., 2013; Mollo et al., 2015; Ubide and Kamber, 2018). The use of an Ar-H_2 mixture as a pressure medium provided the possibility to adjust the required fH_2 in the vessel to attain fO_2 close to the nickel-nickel oxide (NNO) buffer. However, within the sample capsule, the redox state was affected by permeation of hydrogen through the capsule walls driven by different fH_2 between the pressure medium and the capsule interior. This controlled the fugacity of oxygen inside the capsule through the equilibrium reaction of water formation ($H_2 + 1/2O_2 \rightarrow H_2O$). At the beginning of the experiment, the hydrogen fugacity inside the capsule was in disequilibrium with the pressure medium. An initial annealing time of 3 h at $T_{superliquidus} = 1250$ °C was used to homogenize the melt and equilibrate the redox state, but dynamic redox conditions occurred also during decompression and H_2O exsolution. According to ferrous-ferric ratio measurements in glasses (Mollo et al., 2017) and crystal-melt oxygen barometric estimates (Mollo et al., 2018) conducted on similar decompression run products, we can conservatively infer an increase of fO_2 up to NNO + 1.5. Mollo et al. (2015) have calculated that the fO_2 of Etnean magmas ranges from NNO + 1 to NNO + 3, but most of estimates are close to NNO + 1 with a standard deviation of ± 0.8, in agreement with the experimental redox conditions. After the annealing time, the charges were cooled from $T_{superliquidus}$ to $T_{resting}$ in 670 min at the slow rate of 0.3 °C/min (CR_{slow}) for *EXP-0*, in 335 min at the intermediate rate of 0.6 °C/min (CR_{mid}) for *EXP-0.01*, and in 166 min at the fast rate of 1.2 °C/min (CR_{fast}) for *EXP-1* (Table 1). The selected $T_{resting}$ was 1,050 °C, in accordance with direct measurements of the inner temperature of lavas outpoured at Mt. Etna (Armienti et al., 2013). *EXP-0* was kept at 400 MPa and 1,050 °C for 24 h and then isobarically quenched at a rate of 200 °C/s. Conversely, *EXP-0.01* and *EXP-1* were kept at 400 MPa and 1,050 °C for 12 h, isothermally decompressed to 100 MPa by keeping the pressure constant for additional 12 h (Table 1), and finally quenched at a rate of 200 °C/s. Because the cooling and decompression rates (*CR* and *DR*) are responsible for the kinetic growth of crystal frameworks under conditions of melt supersaturation (diffusion-limited growth), the annealing time served to reduce the concentration gradients in the melt adjacent to the crystal surfaces via diffusive relaxation (interface-limited growth) (e.g., Moschini et al., 2021). Also, the degree of undercooling (ΔT) is commensurate to the rate at which the system temperature decreases upon cooling and/or the rate at which the liquidus temperature of the melt increases by exsolution of dissolved H_2O upon decompression (Mollo and Hammer, 2017). The early crystallization of clinopyroxene in *EXP-0*, *EXP-0.01*, and *EXP-1* was driven by a temperature-induced undercooling $\Delta T_T = 23$ °C, calculated as the difference between T_{cpx} and $T_{resting}$ at 400 MPa (Table 1). For *EXP-0.01* and *EXP-1*, a further compositionally-driven decrease of T_{cpx} derived from H_2O exsolution during melt decompression. According to thermodynamic simulations carried out with rhyolite-MELTS, a H_2O-induced additional undercooling $\Delta T_{H2O} = 25$ °C was derived as the difference between T_{cpx} calculated at 400 MPa and T_{cpx} calculated at 100 MPa (Table 1). The condition of $P_{tot} = P_{H2O}$ was denoted by the escape of a fluid phase when the experimental capsules were punctured with a needle at the end of the runs. The recovered capsules were mounted in epoxy and polished for microchemical observations and analyses.

2.2. SEM analysis

Photomicrographs were collected in reflected light using optical microscopy, and in backscattered electron (BSE) mode using field emission gun-scanning electron microscope FE-SEM JEOL JSM-6500F, equipped with an energy-dispersive spectrometer (EDS) detector and installed at the HP-HT Laboratory of Experimental Volcanology and Geophysics of the Istituto Nazionale di Geofisica e Vulcanologia (INGV) in Rome (Italy).

2.3. TEM analysis

Scanning transmission electron microscopy (STEM) imaging and chemical analyses were performed at the Bayerisches Geoinstitut, Universitat Bayreuth (Germany) on a field emission scanning transmission electron microscope FEI Titan G2 80–200 S/TEM, equipped with an energy dispersive X-ray spectrometer (EDS) with 4 Silicon drift detectors, Bruker Quantax. For the TEM sample preparation, a focused ion

Table 1
Experimental conditions. $P_{tot} = P_{H2O}$. *DR*, decompression rate. *CR*, cooling rate. ΔT_T, temperature-induced undercooling. ΔT_{H2O}, H_2O-induced undercooling. T_{cpx}, saturation temperature of clinopyroxene. $T_{resting}$, final target temperature.

Run #	$P_{initial}$ (MPa)	$t_{initial}$ (h)	P_{final} (MPa)	t_{final} (h)	DR (MPa/s)	[1]$H_2O_{dissolved}$ (wt.%)	fO_2 (Buffer)	$T_{superliquidus}$ (°C)	[2]$T_{liquidus}$ (°C)	[2]T_{cpx} (°C)	$T_{resting}$ (°C)	CR (°C/min)	ΔT_T (°C)	ΔT_{H2O} (°C)
EXP-0	400	0	400	24	0	7.6	NNO-NNO + 1.5	1250	1091	1068	1050	0.3	23	0
EXP-0.01	400	12	100	12	0.01	3.1	NNO-NNO + 1.5	1250	1116	1093	1050	0.6	23	25
EXP-1	400	12	100	12	1	3.1	NNO-NNO + 1.5	1250	1116	1093	1050	1.2	23	25

[1] The amount of H_2O dissolved in the melt has been calculated with the equation of state of Duan (2014).
[2] The melt's liquidus temperature and the saturation temperature of clinopyroxene have been calculated with the code rhyolite-MELTS v.1.2.0 of Gualda et al. (2012).

milling machine (FEI Scios DualBeam milling) was used. The thickness of TEM thin foil was ~150 nm. EDS maps were acquired at a resolution of 5–10 nm per pixel and dwell time of 16 μsec per pixel, using a sub-nanometer-sized electron beam with <0.09 nA probe current at 200 kV acceleration voltage. To accumulate statistically significant characteristic X-ray counts in quantitative EDS maps, the total acquisition time was about 60–90 min. During the acquisition, an image drift correction function was activated to prevent artifacts in the profile. To obtain quantitative crystal compositions, Z-number and absorption effects were corrected on the EDS spectrum (Van Cappellen, 1990; Van Cappellen and Doukhan, 1994). For accurate quantification, a natural pyrope-almandine garnet (Pyc-garnet, Prp73Alm17Grs11 in Miyajima et al., 1999) was used as EDS standard for main elements Mg, Al, Si, Ca, and Fe. Other minor elements were quantified with theoretical k-factors (Z-number correction) in the EDS system. Selected area electron diffraction (SAED) patterns of crystals were investigated with conventional bright-field (BF) TEM images and high-angle annular dark-field (HAADF) STEM images.

2.4. Electron microprobe analysis

Major element compositions of zoned clinopyroxene crystals and glasses were determined by an electron probe micro-analyzer (EPMA) JEOL JXA-8200 equipped with five wavelength dispersive spectrometers (WDS) and installed at the at HPHT Lab of INGV-Rome. Analyses were performed on carbon-coated thin sections under high vacuum conditions, using an accelerating voltage of 15 kV and an electron beam current of 7.5nA, with a beam diameter of 2.5 μm. Elemental counting times were 10 s on the peak and 5 s on each of the two background positions, except for chromium, which was measured for 20 s on the peak and 10 s on each background position. Corrections for inter-elemental effects were made using a ZAF (Z: atomic number; A: absorption; F: fluorescence) procedure. Calibration used a range of standards from Micro-Analysis Consultants (MAC; https://www.macstandards.co.uk): albite (Si-PET, Al-TAP, Na-TAP), forsterite (Mg-TAP), augite (Fe-LIF), apatite (Ca-PET), orthoclase (K-PET), rutile (Ti-PET), rhodonite (Mn-LIF) and JEOL Cr metal (Cr-PET). Sodium and potassium were analyzed first to prevent alkali migration effects. Spot analyses defined transects across the crystals with constant spot separation, typically of 2.5 μm. Smithsonian augite and MAC augite were used as quality monitor standards and for the calculation of accuracy and precision. Based on counting statistics, accuracy was better than 1–5% except for elements with abundances below 1 wt%, for which accuracy was better than 5–10%. Precision was typically better than 1–5% for all analyzed elements. For mapping, we used 0.5 μm pixel size and 50 to 150 ms dwell time per pixel, measuring up to 5 elements per analysis (one per diffracting crystal). The area of maps ranged between 1 and 5 mm^2 with a resolution of 310 × 242 to 1024 × 1024 $pixel^2$.

Clinopyroxene major/minor cations and components were determined from microprobe data on the basis of six oxygens, following the calculation scheme described in Mollo et al. (2018). According to the recent work of Di Fiore et al. (2021), the total iron was treated as FeO_t (i.e., Fe_{total}) because gross uncertainties in the estimate of Fe^{3+} arise from electron microprobe analyses and charge balance models imposing perfect stoichiometry (i.e., fictive Fe^{3+} contents). In addition, Di Fiore et al. (2021) found that the stability of $^{fictive}Fe^{3+}$-bearing components is inextricably interrelated to the thermodynamic properties of $CaMgSiO_2$-$CaAl_2SiO_6$-$CaTiAl_2O_6$ multicomponent reciprocal solutions.

2.5. Trace element analysis

Trace element compositions of zoned clinopyroxene crystals and glasses were determined with laser ablation inductively coupled plasma mass spectrometry (LA-ICP-MS), following the mapping technique optimized in Ubide et al. (2015). Analyzed trace elements are representative of relevant geochemical groups in clinopyroxene: transition elements (TE; divalent Ni + Co, trivalent Cr, and tetravalent V), rare earth elements (REE; trivalent La-Lu series + Y, where yttrium is considered as pseudo-lanthanide), high field strength elements (HFSE; tetravalent Ti + Hf + Zr and pentavalent Ta + Nb), large ion lithophile elements (LILE; monovalent Li + K + Rb, and divalent Sr + Ba + Pb), and trivalent Sc. Scandium is not grouped with other elements because its electron configuration does not meet in full the definition of TE (i.e., scandium has no d electrons) and may be also associated with REE for their similar chemical behavior in ore-forming processes. The analyses were carried out at The University of Queensland Centre for Geoanalytical Mass Spectrometry, Radiogenic Isotope Facility (UQ RIF-lab). We used an ASI RESOlution 193 nm excimer UV ArF laser ablation system with a dual-volume Laurin Technic ablation cell and GeoStar Norris software, coupled to a Thermo iCap RQ quadrupole mass spectrometer with Qtegra software. Ablation was performed in ultrapure He to which Ar make-up gas with a trace amount of N_2 was added for efficient transport and to aid ionization. Analyses were conducted using a spot size of 7 × 7 μm, repetition rate of 10 Hz, fluence of 3 J cm^{-2} and translation speed of 7 μm s^{-1}, with 1 μm overlap between rasters (Table S2). This spot size is commonly used for elemental mapping at high spatial resolution and shows good accuracy and precision in both experimental (Mollo et al., 2018, 2020a, 2020b) and natural system (Ubide et al., 2019a). Two analytical runs were carried out to cover all elements of interest without compromising spatial resolution, as detailed in Ubide et al. (2019a). Prior to analysis, the mass spectrometer was tuned with scans on NIST612 glass reference material. Trace element maps were produced using the commercial software Iolite v4 (Paton et al., 2011) in quantitative mode. We used NIST612 as the calibration standards and the concentration of CaO obtained with electron microprobe as the internal standard for clinopyroxene (22.3 ± 0.1 wt%) and glass (10.3 ± 0.3 wt%). Accuracy and precision were monitored using BHVO-2G and BCR-2G as secondary standards (https://georem.mpch-mainz.gwdg.de/), being typically better than 10% and 5%, respectively, under the same analytical conditions as the unknowns (Table S2). Trace element concentrations were extracted from crystal zones and glass using the Monocle add–on for Iolite (Petrus et al., 2017).

2.6. Micro-Raman analysis

Micro-Raman mapping of interface glass was performed at the EVPLab of Roma Tre University (Rome, Italy) using a Jobin Yvon LABRAM HR800 Horiba micro-Raman spectrometer, equipped with an attenuated doubled Nd3:YAG laser (532 nm wavelength) and calibrated using a silicon standard. A motorized stage was used to collect individual Raman spectra, each being associated with a given point on the sample surface. Individual Raman spectra were acquired in rectangular grid patterns with a step size of 1 μm. The operating conditions were 600 grooves/mm grating density, 150 μm confocal hole, 150 μm slit width, 1 × accumulations, and 20 s acquisition time per point. The laser power at the source was 60 mW (0.15 mW on the sample surface). The resulting hyperspectral map is 20 × 40 μm. A nominal spatial resolution of ~1 μm^2 is obtained with the 100 × objective. The backscattered Raman radiation is collected over the 100–4000 cm^{-1} range. The presence of H_2O is detected by normalizing the water band intensity at 3550 cm^{-1} to the spectral intensity at 3000 cm^{-1} selected as a reference for the background signal. This normalization provides information on the presence and relative variation of dissolved H_2O. Quantitative estimations would require more extensive spectral treatment and calibration (e.g., Long correction, baseline subtraction, glass standardization; cf. Di Genova et al., 2017) beyond the aim of this work.

3. Results

3.1. Phase assemblage and clinopyroxene morphology

Clinopyroxene (~15–17 vol%) is the most abundant mineral phase in all run products, with minor presence (~4–6 vol%) of olivine. The crystal content does not substantially change in isobaric and decompression experiments, showing an almost comparable glass amount (~77–81 vol%). Bubbles are also ubiquitous, especially next to the capsule walls.

Reflected light optical photomicrographs (Fig. 1a) show that clinopyroxene crystals from the isobaric experiment *EXP-0* are characterized by polyhedral forms with well-developed planar faces indicative of complete textural maturation under the combined effects of CR_{slow} = 0.3 °C/min and ΔT_T = 23 °C. The formation of interface-limited morphologies can be addressed to the annealing time of 24 h, which was long enough to impose a steady-state clinopyroxene growth via diffusive relaxation phenomena in the low viscosity basaltic melt (cf. Pontesilli et al., 2019). BSE photomicrographs (Fig. 2a) highlight that polyhedral crystals are sector-zoned, with compositionally different growth layers in different crystallographic orientations (i.e., hourglass and prism sectors) as indicated by marked changes in the average atomic number of the crystalline regions (i.e., darker contrasted crystalline regions correspond to higher BSE intensities and *vice versa*).

The morphology of clinopyroxene crystals from the slow decompression experiment *EXP-0.01* is generally sub-euhedral (Fig. 1b). There is also the intergrowth of two or more individuals with different orientations due to a period of cessation of growth after CR_{mid} = 0.6 °C/min and a new stage of growth from a newly supplied interface melt as the result of DR_{slow} = 0.01 MPa/s (Fig. 2b). Irregular boundaries are associated with unsealed, scalloped melt embayments and the entrapment of curvilinear melt inclusions (i.e., ME and MI in Fig. 2b, respectively). Partial destabilization of the advancing crystal–melt interface is caused by kinetic effects resulting from CR_{mid} in combination with DR_{slow}. The entrapment of melt inclusions requires a shift from a diffusion-limited to interface-limited crystallization regime (e.g., Stewart and Pearce, 2004; Blundy and Cashman, 2005; Baker, 2008). After an early stage of rapid crystal growth to form melt embayments, a subsequent period of slow growth was necessary to seal and isolate the embayments during the annealing time. Reaction kinetics at the early stage of growth produce skeletal forms as intrasectoral subsectors that are visible in the central region of the late-growing hourglass and prism sectors (Fig. 2b). Growth sector boundaries are also well identified by the change in orientation of a distinctive concentric band that delineates time-equivalent growth surfaces in the crystal. Both hourglass and prism faces are enclosed by an overgrowth rim showing either planar or irregular boundaries (Fig. 2b). The overall growth history of clinopyroxene generates a composite zoning pattern which is identified in Fig. 2 as sector zoning (SZ), concentric zoning (CZ), intrasectoral subsectors (IS), and overgrowth rims (OR). All these textural attributes will be described in detail in Section 3.2.

Reaction kinetics are exacerbated in the fast decompression experiment *EXP-1*, in which clinopyroxene crystals show elongate shapes with skeletal textures and morphological instability caused by rapid growth conditions (Figs. 1c and 2c). The planar faces are in part substituted by branched protrusions and reentrant faces leading to texturally incomplete forms (Fig. 1c). Larger protrusions develop preferentially at the corners or on the edges of crystals, whilst smaller protrusions occur at

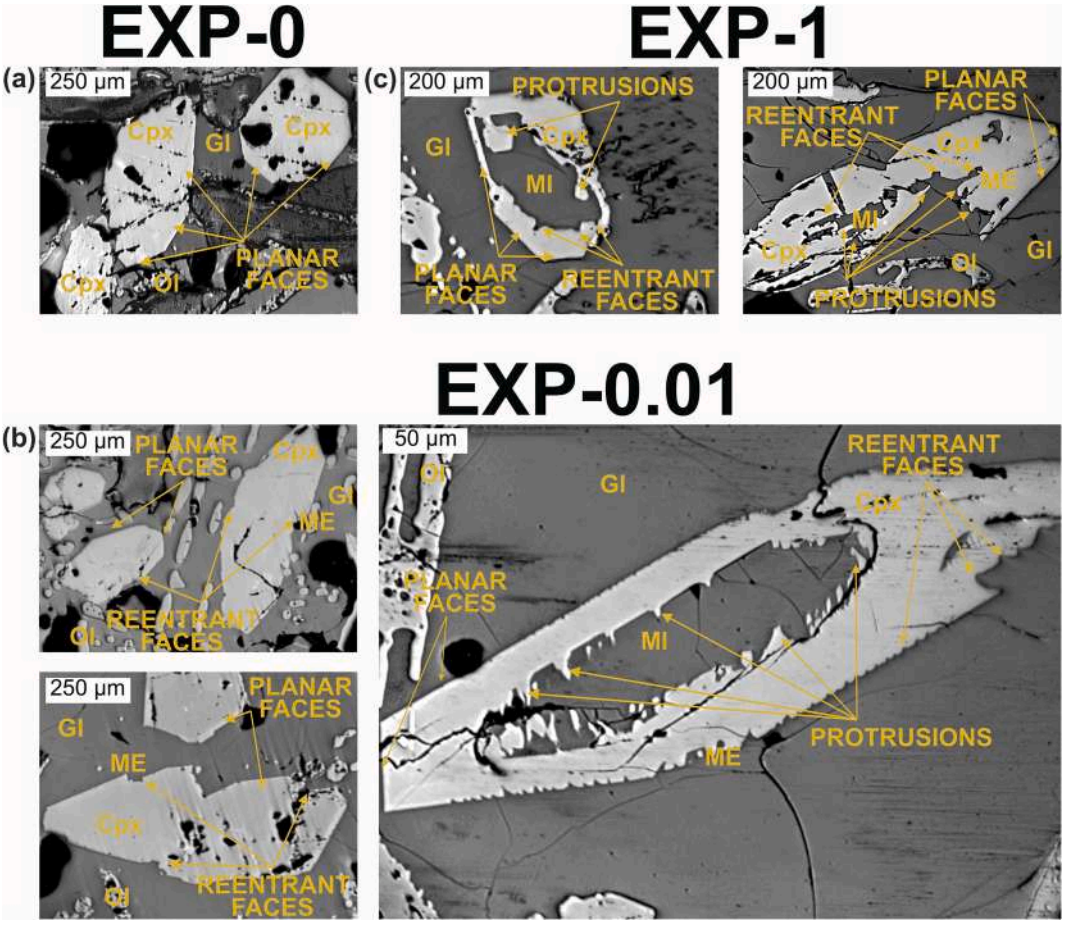

Fig. 1. Reflected light optical photomicrographs of clinopyroxene morphologies from the isobaric experiment *EXP-0* (a), slow decompression experiment *EXP-0.01* (b), and fast decompression experiment *EXP-1* (c). Cpx, clinopyroxene. Ol, olivine, Gl, glass. MI, melt inclusion. ME, melt embayment.

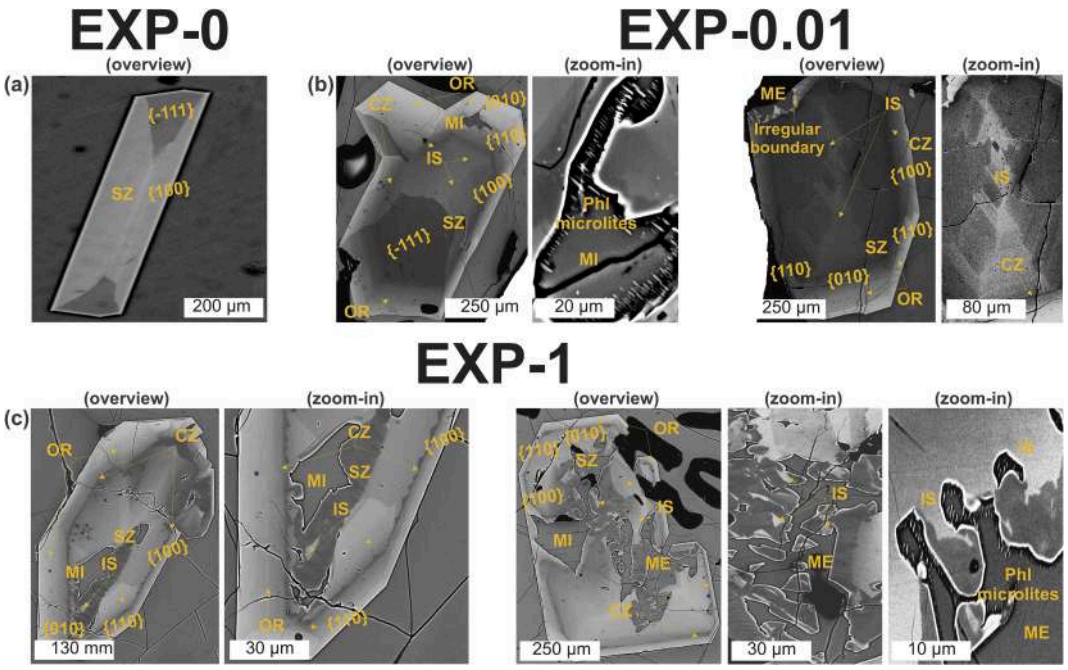

Fig. 2. Back-scattered electron photomicrographs of sector-zoned clinopyroxene crystals from the isobaric experiment *EXP-0* (a), slow decompression experiment *EXP-0.01* (b), and fast decompression experiment *EXP-1* (c). SZ, sector zoning. CZ, concentric zoning. IS, intrasectoral subsector as skeleton (*EXP-0.01*) or patchy zoning (*EXP-1*). OR, overgrowth rim. MI, melt inclusion. ME, melt embayment. Phl, phlogopite.

the center of the face, in which morphological instability is less favored (Fig. 1c). Clinopyroxene crystals attain sub-euhedral habits with rounded hollow sections or incomplete C-shapes containing large melt pockets (Figs. 1c and 2c). Skeletons from *EXP-0.01* are substituted in *EXP-1* by mottled and patchy textures that originate through the combined effects of CR_{mid} = 1.2 °C/min and DR_{fast} = 1 MPa/s. Straight, arcuate, or bended slivers are occasionally observed having a brighter BSE intensity distinctly different from their host sector (i.e., polycrystalline aggregates leading to patchy zoning in Fig. 2c). These slivers define domains of irregular growth directions due to strong kinetic effects and produce clustering or indentation at the boundaries of sector-zoned clinopyroxene crystals (Fig. 2c).

In both isobaric and decompression experiments, the growth of clinopyroxene is occasionally associated with the crystallization of tiny

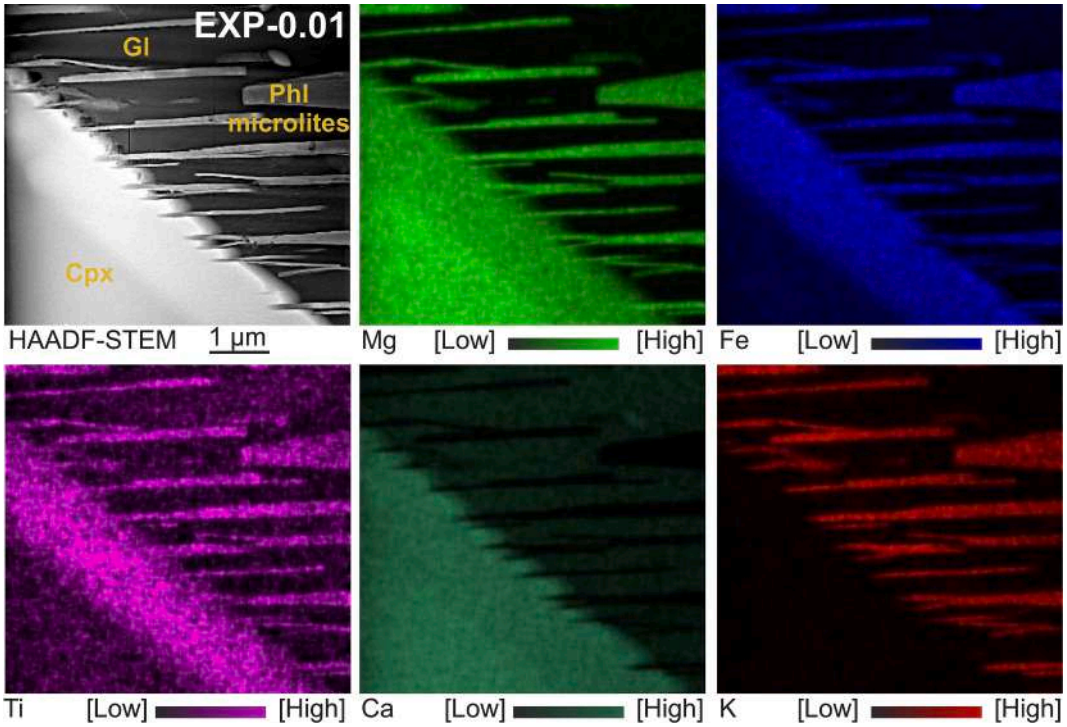

Fig. 3. High-angle annular dark-field scanning transmission electron microscopy imaging at top left and energy-dispersive X-ray spectrometer mapping of phlogopite microlites attaching onto the external surface of clinopyroxene from the slow decompression *EXP-0.01*.

microlites of phlogopite from melt regions next to the clinopyroxene surface and over a maximum length scale of ~10 μm (Fig. 2b, c). These microlites show needle shapes, arrange as lamellar patterns, and systematically emerge from the melt in close proximity to the advancing clinopyroxene surface, also including curvilinear melt embayments and fully enclosed melt inclusions (i.e., ME and MI in Fig. 2b, c). STEM imaging and EDS mapping point out that phlogopite microlites attach onto the external surface of clinopyroxene during the growth of a freshly deposited crystalline layer and are uni-directionally aligned along their major crystallographic axes (Fig. 3).

3.2. Clinopyroxene zoning patterns

The composite zoning patterns of two representative clinopyroxene crystals (i.e., Cpx 1 and Cpx 2) from the slow decompression experiment *EXP-0.01* are resolved in Fig. 4 using electron microprobe chemical maps and transects (AB and CD). Additional chemical maps acquired for two zoned clinopyroxene crystals (Cpx 3 and Cpx 4) from the fast decompression *EXP-1* are presented in Fig. S1.

Sector zoning results from compositional differences among adjacent time-equivalent crystal regions that grow simultaneously to form crystallographically nonequivalent faces (Fig. 4 and Fig. S1). The interface constituting the compositional boundary does not coincide with a

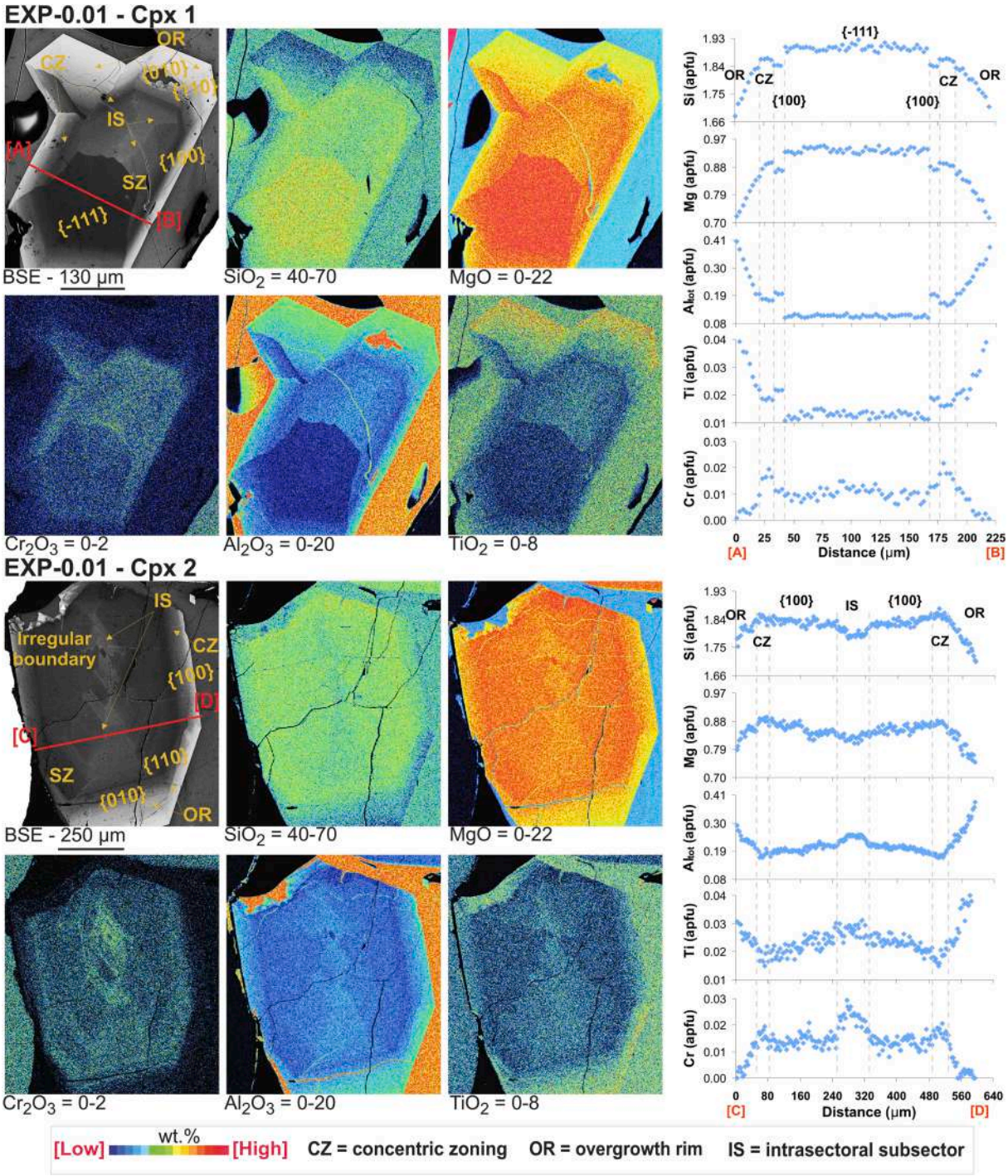

Fig. 4. Electron microprobe chemical maps and transects of two different clinopyroxene crystals from the slow decompression *EXP-0.01*.

growth surface but rather with a growth sector boundary showing intersectoral chemical variations. The geometry of polyhedral faces corresponds to the three-dimensional morphological model described in Leung (1974) for a natural titanaugite from an alkaline olivine basalt, further illustrated in Ubide et al. (2019a, 2019b). Prism sectors {1 0 0}, {1 1 0}, and {0 1 0}, designated for simplicity as {*h k* 0}, grow perpendicular to the *c*-axis and are preferentially enriched in Al_2O_3 + TiO_2, whereas {−1 1 1} hourglass sectors grow along the *c*-axis and incorporate higher proportions of SiO_2 + MgO (Fig. 4 and Fig. S1).

Concentric zoning is found only in clinopyroxene crystals from *EXP-0.01* and *EXP-1* due to the combined effects of cooling and decompression. Time-equivalent growth surfaces form a synchronous and continuous band crosscutting the {−1 1 1} and {*h k* 0} sectors (Fig. 4 and Fig. S1). Planar growth surfaces are better developed in *EXP-0.01* (i.e., CR_{mid} and DR_{slow}) than in *EXP-1* (i.e., CR_{fast} and DR_{fast}) in response to sluggish kinetic effects. The change in orientation of the concentric band identifies the growth sector boundary that separates two different sectors during the attainment of a more stable face morphology with increasing the annealing time (Fig. 4 and Fig. S1). AB and CD transects highlight that the concentric band is markedly enriched in Cr_2O_3 relative to the hourglass and prism faces.

A decompression-induced overgrowth rim occurs in close spatial relationship with the concentric band and its thickness is variable from ~20 to ~80 μm depending on the sector orientation (Fig. 4 and Fig. S1). The overgrowth rim is highly enriched in Al_2O_3 and TiO_2 as larger proportions of incompatible cations are incorporated in the crystal structure (Fig. 4 and Fig. S1). Texturally asymmetric and irregular patterns may also develop at the clinopyroxene rim due to more effective interface kinetics that produce serrate and cuspate boundaries with subparallel orientation (Fig. 4).

An intriguing textural feature of decompression experiments is the occurrence of intrasectoral subsectors (Fig. 4 and Fig. S1), as crystal discontinuities consisting of compositionally distinct subsectors that occur in different regions of the sector in which they are contained (e.g., Paquette and Reeder, 1990). These crystal discontinuities testify to changes in the growth mechanism and originate from an early stage of rapid crystal growth upon the early effect of CR_{mid} (*EXP-0.01*) and CR_{fast} (*EXP-1*). Intrasectoral subsectors do not coincide with a growth sector boundary but rather appear as Cr_2O_3-rich skeletal forms in *EXP-0.01* (Fig. 4). The increased degree of melt supersaturation in *EXP-1* leads to the formation of a composite network of Cr_2O_3-rich intrasectoral subsectors with the shape of slivers delineated by both narrow and arcuate boundaries (i.e., patchy zoning in Fig. S1). Subsequent infilling of these pre-existing crystal frameworks produces hourglass and prism sectors, as melt relaxation phenomena became more effective over the annealing time. Skeletal branches located in the central portion of clinopyroxene crystals from *EXP-0.01* are completely infilled and associated with the textural maturation of polyhedral sectors (Fig. 4). Conversely, the backfill process is markedly incomplete for the early-formed crystal frameworks from *EXP-1*, leading to an immature growth morphology that is characterized by mottled and patchy domains frequently interrupted by glass pockets (Fig. S1).

3.3. Clinopyroxene major/minor cations and components

Fig. 5a shows major-minor cation distributions for the different textural attributes resolved for clinopyroxene crystals from isobaric and decompression experiments. $^{T}Si + {}^{M1}Mg$ decrease and $^{T}Al + {}^{M1}Ti$ increase from *EXP-0* to *EXP-0.01* to *EXP-1*, in response to the kinetically-induced substitutions $[{}^{T}Si, {}^{M1}Mg] \leftrightarrow [{}^{T}Al, {}^{M1}Al]$ and $[2{}^{T}Si, {}^{M1}Mg] \leftrightarrow [2{}^{T}Al, {}^{M1}Ti]$ (Sack and Ghiorso, 1994). Fe_{total} is systematically anti-correlated with ^{M1}Mg and ^{M2}Mg (Table S3) due to the formation of ferroan end-member components in the lattice site of clinopyroxene by multiple substitution reactions $[{}^{M1}Mg, {}^{M2}Mg] \leftrightarrow [{}^{M1}Fe^{2+}, {}^{M2}Fe^{2+}]$, $[{}^{M1}Al] \leftrightarrow [{}^{M1}Fe^{3+}]$, and $[{}^{T}Si, {}^{M1}Mg] \leftrightarrow [{}^{T}Al, {}^{M1}Fe^{3+}]$ (Sack and Ghiorso, 1994).

Decompression experiments show additional textural complexities (concentric bands, overgrowth rims, intrasectoral subsectors), with compositional variations linked to the increase in both cooling rate and decompression rate. For example, the overgrowth rim incorporates a higher number of ^{T}Al, ^{M1}Ti, and ^{M2}Na cations from *EXP-0.01* to *EXP-1* (Table S3). However, the increase in percentage of ^{M2}Na (~18%) remains greatly subordinate to that calculated for ^{T}Al (~57%) and ^{M1}Ti (~65%). Moreover, ^{M2}Ca does not substantially change in the different zoning patterns of clinopyroxene, showing a minimum percentage variation (~2%).

Sectoral differences between hourglass and prism faces are in the order $[{}^{T}Si + {}^{M1}Mg]_{\{-1\,1\,1\}} > [{}^{T}Si + {}^{M1}Mg]_{\{h\,k\,0\}}$ and $[{}^{T}Al + {}^{M1}Ti]_{\{-1\,1\,1\}} < [{}^{T}Al + {}^{M1}Ti]_{\{h\,k\,0\}}$ (Fig. 5a). The compositional data set is also adopted to construct frequency curves that are moderately asymmetric, with right- or left-shoulders and frequency peak positions shifting towards compositions enriched in $^{T}Al + {}^{M1}Ti$ as a function of isobaric and decompression conditions (Fig. 5a).

Concentric bands incorporate higher $^{T}Si + {}^{M1}Mg$ contents than those measured for {*h k* 0} sectors, with the counterbalancing effect of lower $^{T}Al + {}^{M1}Ti$ contents (Fig. 5a). Overgrowth rims form an isolated compositional group that is characterized by the lowest $^{T}Si + {}^{M1}Mg$ and highest $^{T}Al + {}^{M1}Ti$ contents. Frequency curves are almost symmetric with narrow peaks (Fig. 5a).

Clinopyroxene compositions plotted in Fig. 5b are expressed as the sum of diopside (Di; $CaMgSi_2O_6$) and hedenbergite (Hd; $CaFeSi_2O_6$) components, and the sum of Ca-Tschermak (CaTs; $CaAl_2SiO_6$) and CaTi-Tschermak (CaTiTs; $CaTiAl_2O_6$) components. Changes in clinopyroxene components mimic very well the different proportions of $^{T}Si + {}^{M1}Mg$ and $^{T}Al + {}^{M1}Ti$ cations in the different zoning patterns. As a whole, crystal frameworks from isobaric experiment *EXP-0* are preferentially enriched in Di + Hd, whereas those obtained from decompression experiments *EXP-0.01* and *EXP-1* exhibit lower Di + Hd contents, especially at high cooling and decompression conditions (Fig. 5b). The lowest amounts of Di + Hd are measured for the overgrowth rims in concert with the highest proportions of CaTs + CaTiTs components (Fig. 5b). Sector zoning responds to the enrichment and depletion criteria $[Di + Hd]_{\{-1\,1\,1\}} > [Di + Hd]_{\{h\,k\,0\}}$ and $[CaTs + CaTiTs]_{\{-1\,1\,1\}} < [CaTs + CaTiTs]_{\{h\,k\,0\}}$ (Fig. 5b).

3.4. Clinopyroxene trace element mapping

Fig. 6 shows two representative LA-ICP-MS maps for complexly zoned clinopyroxene crystals from decompression experiments *EXP-0.01* and *EXP-1*, in which major (Al), minor (Na and Ti) and trace cations (TE, REE + Y, HFSE, LILE, and Sc) are arranged according to their ionic radius, charge, and host crystallographic site. Following the same approach adopted by Shimizu (1981), the enrichment factor (ε_i, where *i* is the element of interest) has been calculated as the ratio of an element concentration (C_i) in {*h k* 0} relative to {−1 1 1} sectors through the formula ${}^{SZ}\varepsilon_i = {}^{\{h\,k\,0\}}C_i/{}^{\{-1\,1\,1\}}C_i$. This principle has been extended to the enrichment factor of cations in concentric zones (${}^{CZ}\varepsilon_i = {}^{CZ}C_i/{}^{SZ}C_i$) and overgrowth rims ($\varepsilon_{OR} = {}^{OR}C_i/{}^{SZ}C_i$) relative to their average concentrations in prism and hourglass faces [i.e., $({}^{\{h\,k\,0\}}C_i + {}^{\{-1\,1\,1\}}C_i)/2$]. For simplicity, an average enrichment factor has been calculated for groups of isovalent cations using data listed in Table S4.

For cations hosted in the M1-site, ${}^{SZ}\varepsilon_{HFSE5+}$ (~3.8) > ${}^{SZ}\varepsilon_{HFSE4+}$ (~2.0) > ${}^{SZ}\varepsilon_{V}$ (~1.6) > ${}^{SZ}\varepsilon_{Sc}$ (~1.1), with the enrichment factors of Cr, Ni, and Co close to unity due to the lack of substantial compositional variations for these transition cations between {*h k* 0} and {−1 1 1} sectors (Fig. 6). As $^{T}Al + {}^{M1}Ti$ increase in the coordination polyhedra of {*h k* 0} sectors, smaller and more charged trace cations are preferentially incorporated via Tschermak substitutions. Also, ${}^{SZ}\varepsilon_{REE+Y}$ (~1.5) > ${}^{SZ}\varepsilon_{LILE1+}$ (~1.2) for cations hosted in the M2-site, and ${}^{SZ}\varepsilon_{LILE2+}$ is below unity.

The distribution of trace cations in concentric zones is generally similar to that observed for {−1 1 1} sectors, so that concentric zones are

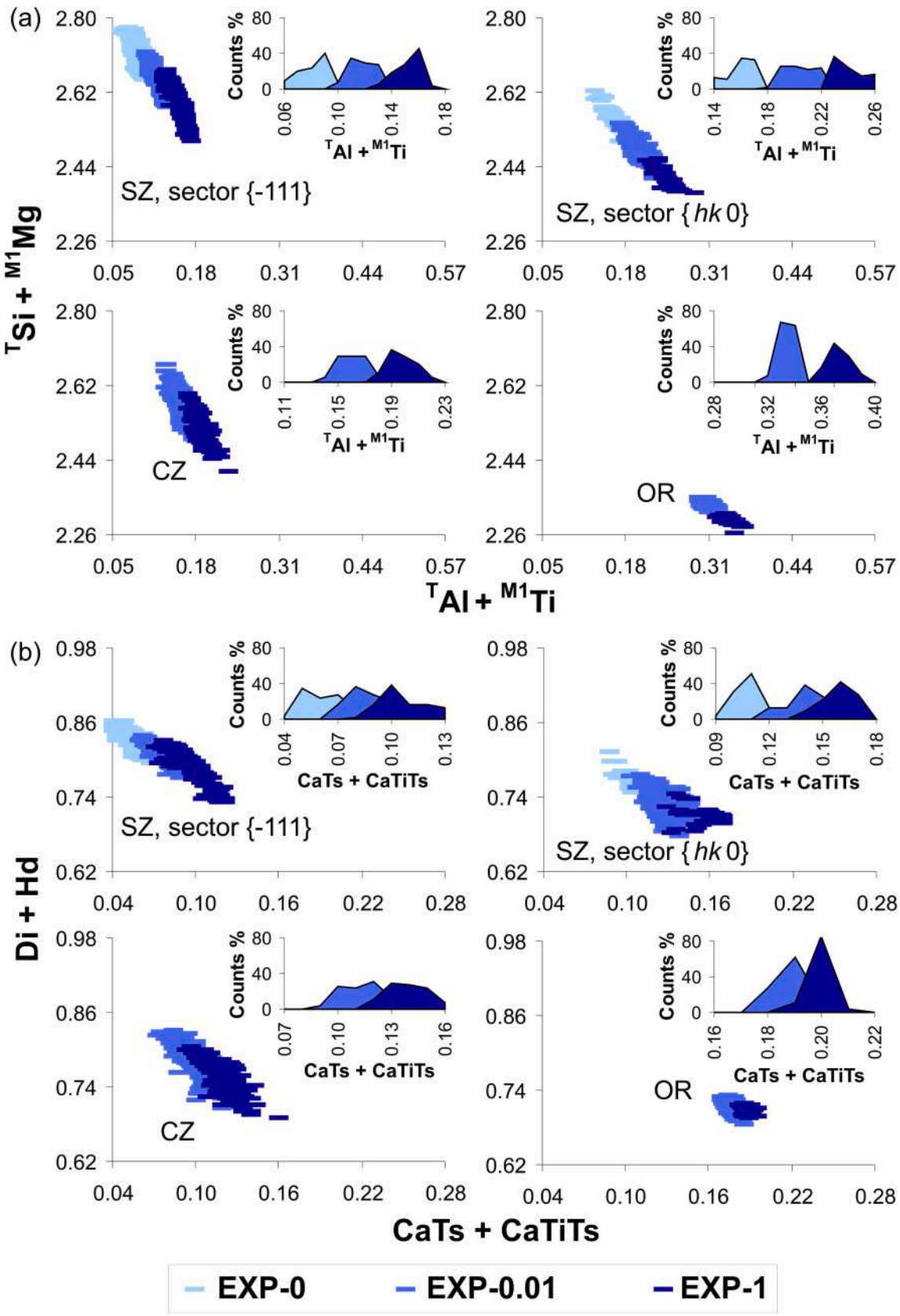

Fig. 5. Clinopyroxene major-minor element oxides (a) and components (b) from the isobaric experiment EXP-0, slow decompression experiment EXP-0.01, and fast decompression experiment EXP-1. Clinopyroxene cations and components have been determined from microprobe data on the basis of six oxygens, following the calculation scheme described in Mollo et al. (2018). Inserts show frequency curves that are obtained for cations and components. Di, diopside. Hd, hedenbergite. CaTs, Ca-Tschermak. CaTiTs, CaTi-Tschermak.

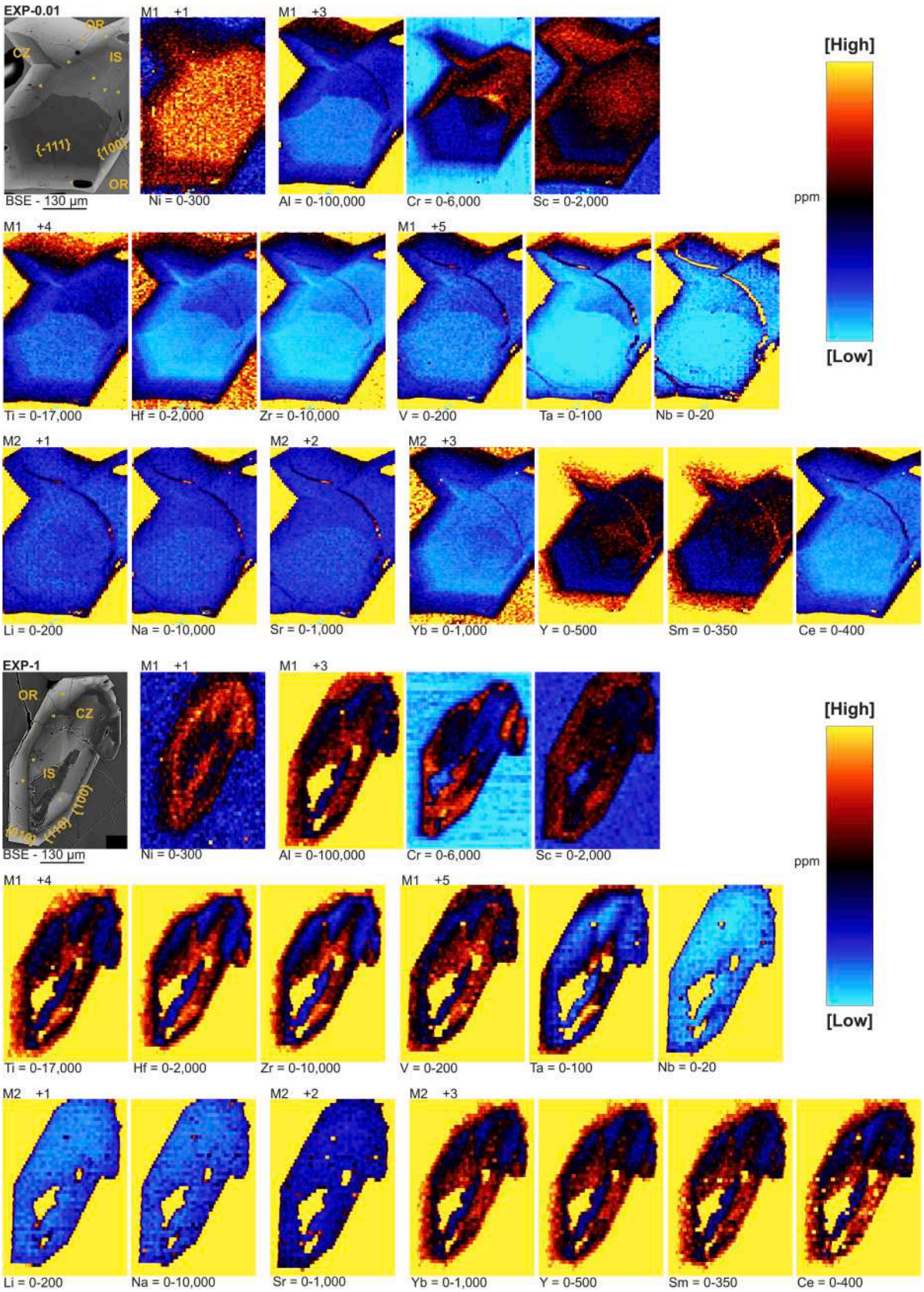

Fig. 6. Laser ablation inductively coupled plasma mass spectrometry maps for clinopyroxene crystals from slow (*EXP-0.01*) and fast (*EXP-1*) decompression experiments. Major (Al), minor (Na and Ti) and trace cations (TE, REE + Y, HFSE, LILE, and Sc) are arranged according to their ionic radius, charge, and host crystallographic site. TE, transition elements. REE, rare earth elements. HFSE, high field strength elements. LILE, large ion lithophile elements.

more reluctant than {*h k* 0} sectors to incorporate incompatible REE + Y and HFSE (Fig. 6). However, Cr, Ni, and Co transition cations concentrate at high proportions in the octahedral site of synchronous bands, in the order $^{CZ}\varepsilon_{Cr}$ (~2.4) > $^{CZ}\varepsilon_{Ni}$ (~1.3) > $^{CZ}\varepsilon_{Co}$ (~1.2) and regardless of {−1 1 1} and {*h k* 0} crystallographic configurations (Fig. 6).

Among all the different textural attributes observed for clinopyroxene crystals, the overgrowth rims from decompression experiments *EXP-0.01* and *EXP-1* are dramatically enriched in trace cations incompatible with the lattice site of clinopyroxene (Fig. 6). This compositional change accounts for the very high proportion of Tschermak components (Fig. 5b) attained by (1) upon kinetic effects controlled by fast cooling and decompression rates and (2) the late crystallization stage from more differentiated residual melts. As a general rule, $^{OR}\varepsilon_{HFSE5+}$ (~2.6) > $^{OR}\varepsilon_{HFSE4+}$ (~1.8) > $^{OR}\varepsilon_{V}$ (~1.7) > $^{OR}\varepsilon_{Sc}$ (~1.1) for the M1-site, whereas $^{OR}\varepsilon_{REE+Y}$ (~1.8) > $^{OR}\varepsilon_{LILE1+}$ (~1.4) and $^{OR}\varepsilon_{LILE2+}$ < 1 for the M2-site. Values calculated for $^{OR}\varepsilon_{Cr}$, $^{OR}\varepsilon_{Ni}$, and $^{OR}\varepsilon_{Co}$ are also below unity, as the melt surrounding the overgrowth rim is greatly depleted in mafic components by cooling- and decompression-induced crystallization.

Together, elemental mapping via LA-ICP-MS (Fig. 6) and electron microprobe (Fig. 4) punctuate that the very high concentration of Cr in intrasectoral subsectors is conjoined with an increased amount of REE + Y, HFSE, Sc, and V contents. However, differently from concentric zoning, the uptake of Cr in the M1-site of early-formed skeletal forms and disequilibrium crystalline frameworks are independent of Ni and Co concentrations (Fig. 6). The CD transect displayed in Fig. 4 highlights that Cr concentrates in intrasectoral subsectors as [^{T}Si, ^{M1}Mg] ↔ [^{T}Al,

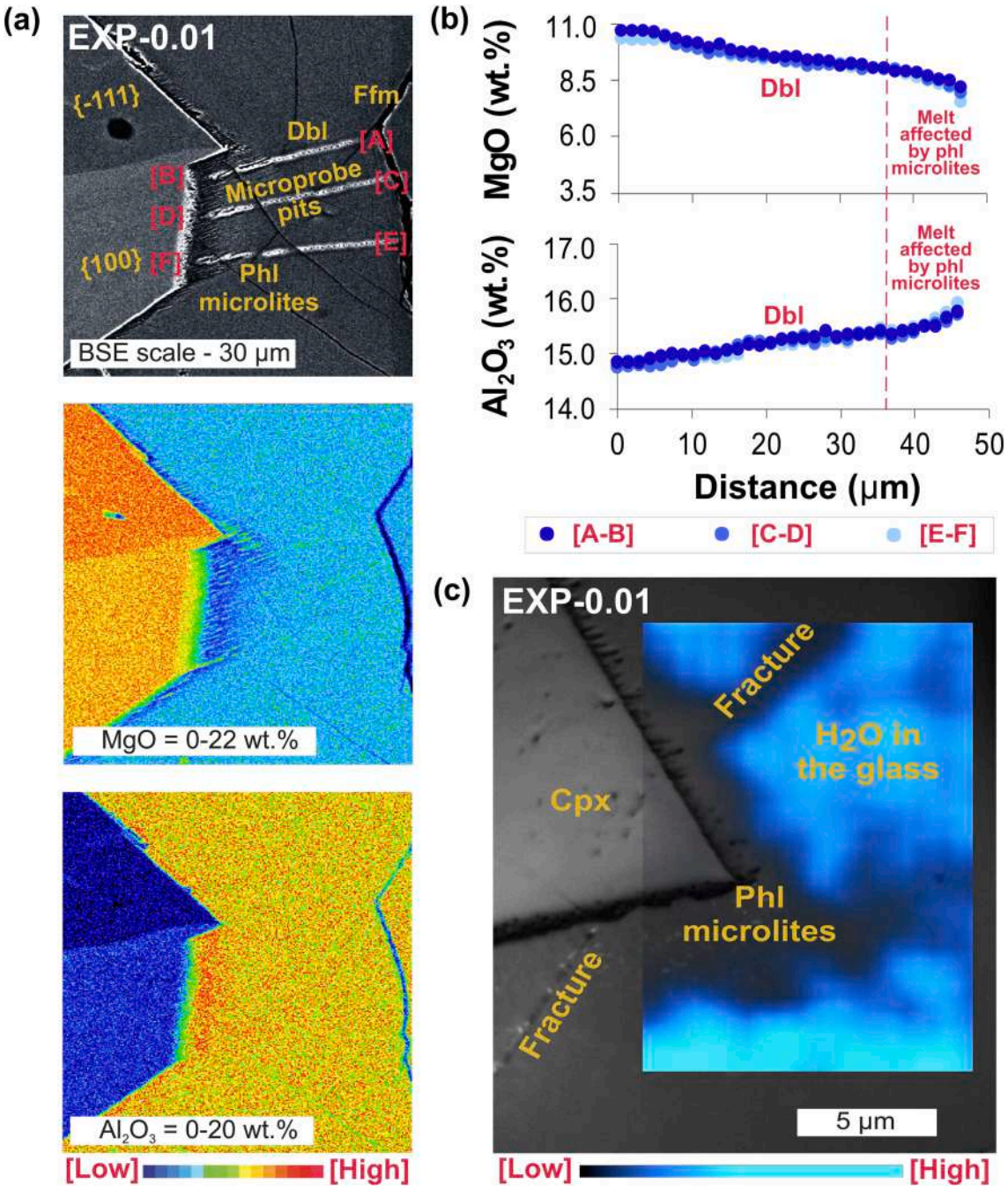

Fig. 7. Diffusion of chemical components in the melt adjacent to a sector-zoned clinopyroxene crystal from the slow decompression experiment *EXP-0.01*. Back-scatted electron image of clinopyroxene and melt (a). Electron microprobe maps (a) and transects (b) of MgO and Al_2O_3 chemical components. Micro-Raman mapping showing H_2O concentration gradients in the melt (c). Dbl, diffusive boundary layer. Ffm, far field melt. Cpx, clinopyroxene. Phl, phlogopite.

^{M1}Cr], according to the same coupled substitutions [^{T}Si, ^{M1}Mg] ↔ [^{T}Al, ^{M1}Al] and [2^{T}Si, ^{M1}Mg] ↔ [2^{T}Al, ^{M1}Ti] documented for Tschermak-rich crystal zones.

4. Discussion

4.1. Melt diffusive boundary layer and clinopyroxene growth rate

During the kinetic growth of sector-zoned clinopyroxene crystals a diffusive boundary layer develops in the basaltic melt next to the clinopyroxene surface (Fig. 7), testifying to supersaturation phenomena imputable to the disparity between the rate at which the crystal surface advances and the rate of cation diffusion in the melt (Kirkpatrick, 1981; Lasaga, 1997; Sunagawa, 2005). A supersaturated melt represents a metastable system evolving towards bulk thermodynamic equilibrium as relaxation phenomena become increasingly effective by lowering any concentration gradient at the crystal-melt interface. Thermodynamic equilibrium requires that the rate at which atoms are attached from the melt onto the crystalline layer is completely balanced by the reverse process of detachment (Kirkpatrick, 1981; Lasaga, 1997; Sunagawa, 2005). On the grounds of this corollary, the condition of melt supersaturation corresponds to the driving force for crystallization related to the Gibbs potential difference throughout the crystal-melt interface (Tsuchiyama, 1985; Kouchi et al., 1983).

Electron microprobe maps (Fig. 7a) and transects (Fig. 7b) from the slow decompression *EXP-0.01* show an example of MgO and Al_2O_3 chemical variations in the diffusive melt that extends from the far field (relaxed) melt unaffected by chemical gradients towards the interface (supersaturated) melt, which is adjacent to the crystal surface and supplies chemical nutrients to the newly formed crystalline layer (all data are reported in Table S5). The thickness of the diffusive fields is in the range ~40–80 μm and its length scale is compatible with thin diffusive boundary layers reported for naturally cooling systems (see Watson and Müller, 2009 and reference therein). Mg cations compatible with the crystal lattice are depleted in the melt near the crystal edge, whereas Al cations incompatible with the advancing crystal surface are enriched in the adjacent melt (Fig. 7a, b). Al_2O_3 enrichments and MgO depletions conform to the coupled substitution [^{T}Si, ^{M1}Mg] ↔ [^{T}Al, ^{M1}Al] governing the compositional evolution of clinopyroxene (Fig. 7a) and the early observation that kinetic factors may produce sector zoning in clinopyroxene crystals via diffusive effects in the growth medium (Hollister and Gancarz 1971; Nakamura 1973; Leung 1974; Dowty 1976, 1977). Sectoral arrangements (Figs. 2 and 4) and compositions (Fig. 5) identical to those presented here have been largely documented for natural (Downes, 1974; Duncan and Preston, 1980; Ubide et al., 2019a, 2019b; Mollo et al., 2020b) and experimental (Masotta et al., 2020; MacDonald et al., 2022) sector-zoned titanaugite crystals growing from mafic alkaline magmas, such as those erupted at Mt. Etna.

Following the calculation scheme of Putirka (2016), the parameter *NBO/T* is determined as the number of non-bridging oxygens (*NBO*) per tetrahedral (*T*) cations (Table S5). The calculation also considers the amount of H_2O estimated *by the difference method* of Devine et al. (1995) as: $H_2O_{EMPA} = 100 - \Sigma_{EMPA}$, where Σ_{EMPA} is the sum of anhydrous oxide components measured in the glass with microprobe. For dissolved H_2O contents up to ~7.5 wt%, data from recent works on alkaline silicate glasses point out that values of H_2O_{EMPA} are overestimated by only ~10% in comparison to more accurate micro-Raman analyses (Bonechi et al., 2022; Moschini et al., 2023). The magnitude of *NBO/T* shows little changes from the far field melt (~1.37–1.48) towards the interface melt (~1.34–1.55) as the result of two counterbalancing effects: (1) melt polymerization as the number of network-modifying divalent cations decreases (Fig. 7b) and (2) melt depolymerization as the amount of dissolved H_2O increases (Fig. 7c). By examining the microprobe analyses of interface melts that coexist with clinopyroxene sectors, concentric bands, and overgrowth rims, the melt feeding the growth of different crystalline layers is constantly buffered to the composition of a basalt, with $SiO_2 \approx 48.1–51.8$ wt% and $Na_2O + K_2O \approx 3.9–4.0$ wt% (Table S5).

Some arguments suggest that the onset of phlogopite nucleation from the diffusive melt is driven by the kinetic growth of clinopyroxene: (1) phlogopite is a hydrous mineral bearing abundant hydroxyl groups aligned in multiple layers and it seems unlikely that phlogopite develops as a quench phase during melt decompression and H_2O exsolution, (2) phlogopite microlites systematically develop in close proximity of the clinopyroxene surface rather than as isolated crystals dispersed in the far field melt (Fig. 2b, c), and (3) phlogopite microlites attach onto the clinopyroxene surface (Fig. 3), perhaps in response to heterogeneous nucleation mechanisms and free energy reduction imposed by the pre-existing clinopyroxene substrate. Moreover, whether or not phlogopite crystallization occurs, the magnitude and sign of chemical gradients for a specific oxide component do not substantially change in the diffusive melt. Tiny phlogopite microlites crystallize within a restricted melt region and show a very low mass fraction relative to that of large clinopyroxene crystals. This effect is quantified by estimating the mass fraction of crystalline phases from the total volume (V) and density (ρ) of clinopyroxene ($V_{cpx} \approx 8.5 \times 10^{-4}$ cm^3 and $\rho_{cpx} \approx 3.3$ g/cm^3) and phlogopite ($V_{phl} \approx 7.9 \times 10^{-9}$ cm^3 and $\rho_{phl} \approx 2.8$ g/cm^3), respectively. The resulting mass fraction of phlogopite ($M_{phl} \approx 1.7 \times 10^{-6}$) is about five orders of magnitude lower than that ($M_{cpx} \approx 0.16$) of clinopyroxene. A direct consequence of this calculation is that the velocity at which the clinopyroxene surface advances in the melt is the main mechanism controlling interface reactions and the degree of supersaturation, as the crystal growth rate largely exceeds the diffusion of cations in the decompressed melt by promoting compositional gradients in the glassy matrix immediately adjacent to sector-zoned crystals (Fig. 7a).

Micro-Raman mapping carried out for the quenched glass from the slow decompression experiment *EXP-0.01* points out that H_2O concentration gradients extend in the melt surrounding the clinopyroxene sectors (Fig. 7c). H^+ behaves as an incompatible element in clinopyroxene and the partition coefficient of H_2O between clinopyroxene and melt is much lower than unity (i.e., 10^{-2}–10^{-3}; O'Leary et al., 2010). The advancement of clinopyroxene surfaces is therefore expected to be faster than the diffusion length distance of H_2O in the basaltic melt, so that H_2O diffusion gradients develop in proximity of the clinopyroxene surface favoring the formation of phlogopite microlites (Fig. 7). For the isobaric experiment, the clinopyroxene growth rate is estimated through one of the most common methods reported in literature (e.g., Pontesilli et al., 2019 and references therein): $G = (L \times W)/(2\,t)$, where L and W are the mean length and width, respectively, whereas t is the annealing time and the factor 2 refers to the growth of a half-crystal during face advancement. This calculation method returns $G = \sim 2.0 \pm 0.2 \times 10^{-7}$ cm/s for clinopyroxene crystals with L and W in the ranges ~0.03–0.06 and ~0.02–0.03 cm, respectively. Because of the lack of a steady clinopyroxene growth in decompression experiments, it is not possible to exactly quantify the growth rate of one crystal surface relative to another (cf. Albarede and Bottinga, 1972), as complexly zoned crystals result from superimposition of different growth histories for {−1 1 1} and {h k 0} sectors, intrasectoral subsectors, concentric bands, and overgrowth rims. Using the model of Zhang et al. (2017) and its associated calibration error, the diffusivity of H_2O in the basaltic melt at $T_{resting} = 1050$ °C corresponds to 26.5 ± 0.5 m^2/s in natural logarithm. According to the calculation scheme reported in Watson and Liang (1995), the square root of H_2O diffusivity multiplied by the experimental time returns a mean diffusive transport distance of ~550 ± 150 μm. By equating the diffusion time with the growth time (cf. Watson and Liang, 1995), it results that the velocity at which one hypothetical clinopyroxene surface advances in the basaltic melt should be faster than $\sim 6.4 \pm 1.8 \times 10^{-7}$ cm/s. This conservative estimate matches with the growth rate of ~10^{-7} cm/s experimentally measured by Masotta et al. (2020) for sector-zoned clinopyroxene crystals growing from an Etnean trachybasaltic melt upon undercooling conditions of 23–32 °C. For the same melt composition, clinopyroxene growth rates on the order of ~10^{-7} cm/s have been resolved by in situ 4D (three dimensions + time)

X-ray microtomography for euhedral crystal morphologies approaching their final equilibrium size under small undercoolings ≤20 °C (Arzilli et al., 2022). In the system $CaMgSi_2O_6$-$CaTiAl_2O_6$, Kouchi et al. (1983) measured growth rates on the order of ~10^{-7}–10^{-6} cm/s for a single seed of sector-zoned clinopyroxene suspended in a melt that was undercooled at rates ≤25 °C, also denoting that {−1 1 1} sector grow faster than {*h k* 0} sector by a factor 2 at undercoolings ≤18 °C and by a factor 10 at the undercooling of 25 °C.

4.2. Clinopyroxene-melt trace element partitioning

As illustrated in Fig. 5, clinopyroxene growth kinetics are associated with the formation of a diffusive boundary layer at the crystal–melt interface from which chemical components are directly incorporated into the lattice site (e.g., Leung, 1974; Dowty, 1976, 1977). The structural and chemical characteristics of the crystal surface are strictly controlled by the interface melt supplying nutrients to the advancing crystalline layer, whereas in the far field melt all chemical gradients cease and the system returns to homogeneous concentrations (e.g., Mollo et al., 2013; Lang et al., 2021, 2022). This principle conforms to the early definition given by Albarede and Bottinga (1972) for the calculation of a partition coefficient, as the ratio between the composition of a freshly deposited crystalline layer and the composition of the melt portion right adjacent to this layer. In addition, the mass fraction of

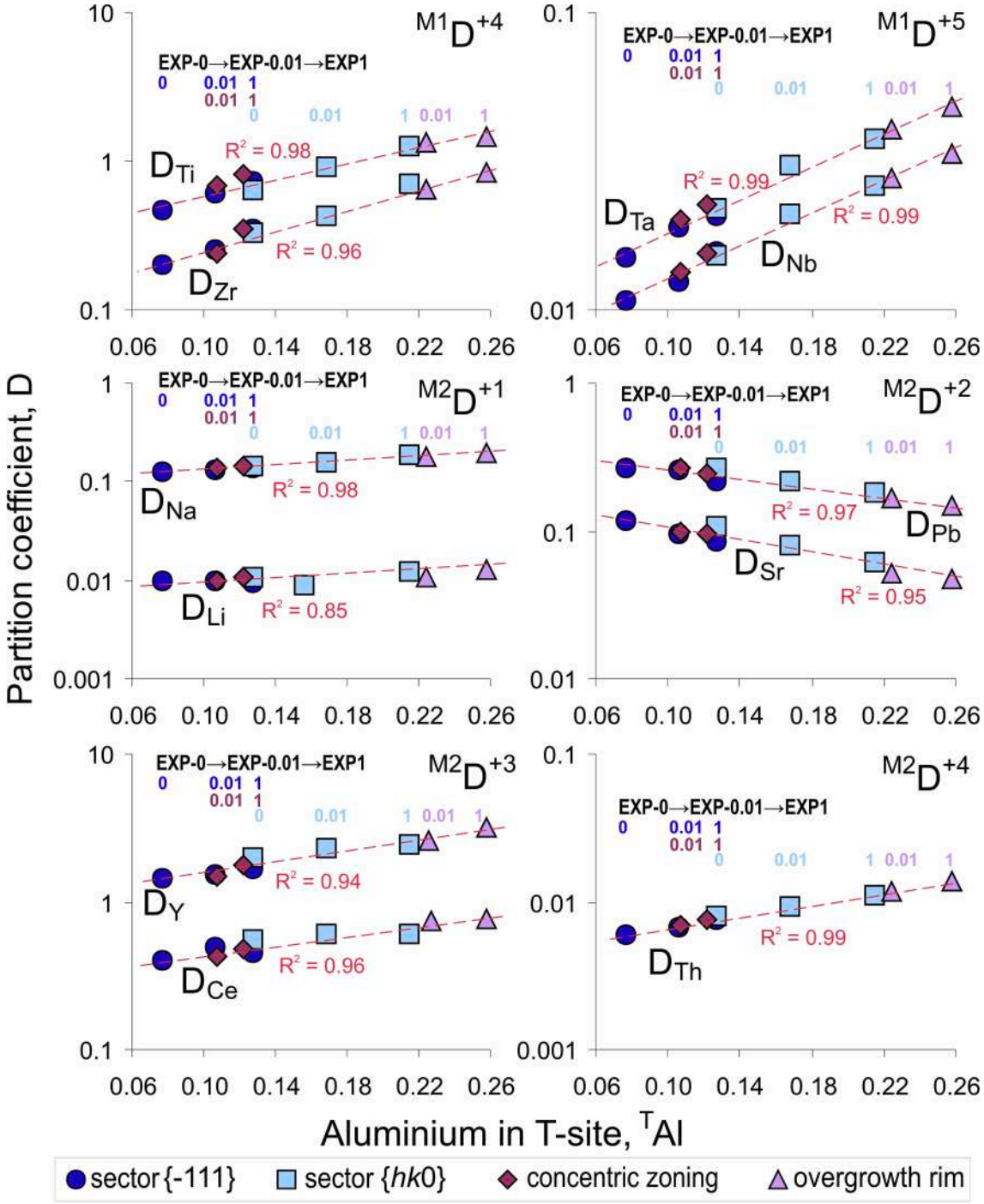

Fig. 8. Variation of apparent partition coefficients determined for minor and trace cations hosted in M1- and M2-sites of different clinopyroxene zones as a function of aluminium in T-site. Most of error bars are within the symbols and are not plotted for the sake of clarity.

phlogopite microlites is orders of magnitude lower than that of clinopyroxene, therefore any departure from bulk melt composition is expected to be marginal and uninfluential for partition coefficients calculated using interface melt regions unaffected by phlogopite crystallization. On this basis, back-scattered electron imaging are used to carefully resolve phlogopite-free interface melts and perform spot analyses as close to the clinopyroxene surface as possible, at a maximum distance to the interface of ~10 μm. Apparent partition coefficients ($D_i = I^{cpx}/I^{melt}$, where I is the cation concentration on a weight basis) for the overgrowth rims have been calculated against the composition of the adjacent glass. D_i for concentric bands and {−1 1 1} and {h k 0} sectors isolated in the inner part of clinopyroxene have been calculated against the composition of phlogopite-free melt embayments and melt inclusions in close proximity with these crystal layers. All values of D_i are listed in Table S6 together with their standard deviations. The legitimacy and reliability of our partitioning data set will be discussed later in Section 4.3 by virtue of thermodynamic and energetic considerations based on the change in cation charge and ionic radius.

Fig. 8 summarizes the variation of some key apparent partition coefficients determined for minor and trace cations hosted in M1- and M2-sites of clinopyroxene, and representative of different geochemical groups. As the amount of ^{T}Al increases in the lattice site of crystals from *EXP-0* to *EXP-0.01* to *EXP-1*, we observe that $^{M1}D^{4+}$ (i.e., D_{Ti} and D_{Zr} for $HFSE^{4+}$) and $^{M1}D^{5+}$ (i.e., D_{Nb} and D_{Ta} for $HFSE^{5+}$) increase for cations hosted in the M1-site (Fig. 8). Similarly, $^{M2}D^{1+}$ (i.e., D_{Na} and D_{Li} for $LILE^{1+}$), $^{M2}D^{+3}$ (i.e., D_{Ce} and D_{Y} for REE + Y^{3+}), and $^{M2}D^{4+}$ (i.e., D_{Th} for tetravalent actinide series) increase for cations hosted in the M2-site (Fig. 8). The net charge on the M2-site is the same in both $CaMgSi_2O_6$ and $CaAl_2SiO_6$ end-members, but $^{M2}D^{2+}$ (i.e., D_{Sr} and D_{Pb} for $LILE^{2+}$) decreases as the proportion of diopside-like structural sites decreases through the mutual substitutions [^{T}Si, ^{M1}Mg] ↔ [^{T}Al, ^{M1}Al] and [2^{T}Si, ^{M1}Mg] ↔ [2^{T}Al, ^{M1}Ti] (Hill et al., 2000; Adam and Green, 2006; Mollo et al., 2013, 2020a). Linear regression analysis indicates that the magnitude of D_i for small and highly charged cations is tightly correlated with ^{T}Al (R^2 = 0.96–0.99; Fig. 8), responding to charge balance compensation mechanisms that enhance the stability of different local configurations into the clinopyroxene structure, such as $(REE, Y)^{3+}MgAlSiO_6$, $Ca(HFSE)^{4+}Al_2O_6$, and $CaMg(HFSE)^{5+}AlO_6$ (Lindstrom 1976; Ray et al. 1983; Hart and Dunn 1993; Forsythe et al. 1994; Lundstrom et al. 1994, 1998; Skulski et al. 1994; Blundy et al. 1998; Hill et al., 2000, 2011; Wood and Trigila, 2001).

Owing to the concurrent increase of aluminium and sodium in the clinopyroxene structure (Table S3), additive effects of these two cations on D_i as the number of charge balance configurations increases in M1- and M2-sites cannot be excluded (Lundstrom et al., 1994; Blundy and Dalton, 2000; Bennett et al., 2004; Marks et al., 2004). For example, the entry of ^{M2}Na may favor the formation of $Na_{0.5}(REE,Y)^{3+}_{0.5}MgSi_2O_6$, $Na_{0.5}(REE,Y)^{3+}_{0.5}Al_2SiO_6$, $Na(HFSE)^{4+}AlSiO_6$, and $Na(HFSE)^{5+}Al_2O_6$ components (Blundy et al. 1998; Schosnig and Hoffer 1998; Wood and Blundy 2001; Bennett et al. 2004; Marks et al. 2004; Francis and Minarik 2008; Beard et al., 2019). However, thermodynamic calculations based on diopside-jadeite melting (or fusion) reactions indicate that the effect of pressure on the partitioning of trace cations is almost negligible at $P <$ 500 MPa (Wood and Blundy, 1997; Blundy and Wood, 2003). This observation is supported by the small change of ^{M2}Na relative to ^{T}Al in clinopyroxene zoning patterns (see Section 3.4). As previously discussed in Mollo et al. (2020a), only a low fraction of charge-neutral local configuration is attributable to ^{M2}Na as a charge-balancing cation for Na-poor crystals from this study (Na_2O = 0.17–0.69 wt%) compared to Na-rich crystals synthesized from basaltic melts at mantle pressure (Na_2O = 2.2–13.5 wt%; data from Klemme et al., 2002; Bennett et al., 2004; Marks et al., 2004) and tephriphonolitic to phonolitic melts at crustal pressure (Na_2O = 1.0–11.5 wt%; data from Beard et al., 2019).

The magnitude of D_{REE+Y} and D_{HFSE} calculated for {−1 1 1} and {h k 0} sectors from the isobaric experiment is lower than that measured for decompression experiments and is observed to increase with increasing cooling and decompression rates (Fig. 8). Partitioning kinetics of trace cations are therefore markedly exacerbated in decompression experiments due to the composite growth history of clinopyroxene. Under such dynamic conditions, the formation of Al-O-Al linkages in the short-range structural arrangement of the clinopyroxene lattice causes preferential incorporation of REE + Y in Tschermak-rich sectors as the valence of charge-balancing cations in adjacent sites increases (Wood, 1976; Wood and Blundy, 1997). Short-range ordering of tetrahedral Si-Al leads to an increased statistical proportion of M2-sites where the local charge of the central cation is 3+ rather than 2+ (Wood and Blundy, 2001; Blundy and Wood, 2003; Sun and Liang, 2012; Mollo et al., 2013; Scarlato et al., 2014; Ubide et al., 2019a). At the same time, the mutual substitutions [^{T}Si, ^{M1}Mg] ↔ [^{T}Al, ^{M1}Al] and [2^{T}Si, ^{M1}Mg] ↔ [2^{T}Al, ^{M1}Ti] enhance the entry of highly charged HFSE onto the M1-site of Tschermak-rich sectors due to greater ease of charge neutralization relative to low charged cations (Wood and Trigila, 2001; Hill et al., 2000, 2011; Mollo et al., 2018, 2020a; Bonechi et al., 2021; MacDonald et al., 2022).

Partition coefficients calculated for concentric bands and {−1 1 1} sectors generally overlap (Fig. 8), suggesting that the incorporation mechanisms are controlled by the same clinopyroxene structural configurations and partitioning energetics (Hill et al., 2000, 2011; Bennett et al., 2004; Mollo et al., 2013, 2020b). In contrast, values of D_{Ni} (~1.2–1.3), D_{Co} (~1.2), and D_{Cr} (~3.5–4.6) from concentric bands are systematically higher than those measured for {−1 1 1} sectors and other crystal zones (Table S6). Cr, Ni, and Co belong to the first series transition metals and have high crystal field stabilization energies in octahedral coordination ($^{oct}CFSE$). Following the early suggestion of Duncan and Preston (1980), the relation $^{oct}CFSE_{Cr}$ (224.7 kJ/mole) > $^{oct}CFSE_{Ni}$ (122.2 kJ/mole) > $^{oct}CFSE_{Co}$ (61.9 kJ/mole; data from White, 2013) strongly controls the uptake of trace cations in the M1-site of concentric bands in the order $D_{Cr} > D_{Ni} > D_{Co}$. Crystal field effects are particularly marked for the incorporation of Cr in M1-site due to its highest $^{oct}CFSE$ relative to other transition elements (Figs. 4 and 6). Cr occupies only the regular M1 polyhedron of clinopyroxene and is reluctant to Jahn-Teller effects arising from the removal of orbital degeneracy by polyhedron distortions (Jahn and Teller, 1937). Note that in terrestrial magmas within the crust Cr predominates as Cr^{3+}, whereas Cr^{2+} occupies the lattice site of minerals from meteoritic and lunar systems (Burns, 1975; Akasaka et al., 2019). Thus, the incorporation of Cr in clinopyroxene is independent of the effect of fO_2 on the crystallization of crustal magmas, as Cr^{2+} is stable only at very low oxygen fugacity conditions and mantle pressures (Akasaka et al., 2019 and references therein).

For a single cooling or undercooling step, the growth rate of clinopyroxene linearly decreases as diffusive relaxation proceeds over the annealing time, so that the diffusion of cations across the crystal-melt interface decreases steadily until it reaches zero (e.g., Pontesilli et al., 2019). However, this is not the case in our experiments. There is compelling circumstantial evidence that Cr-Ni-Co-rich concentric bands in our experiments record changes in the environment of growth over time (Figs. 2, 4, and 6). More specifically, changes in the velocity of the advancing crystal surface and the transport of cations in the melt occur by superimposition of different cooling and decompression regimes. As a result, the thermodynamic driving force for crystal growth shifts from a temperature-dependent ΔT_T to a composition-dependent ΔT_{H2O} caused by melt decompression and H_2O exsolution. The viscosity increase accompanying H_2O exsolution inhibits the diffusion of crystal-forming components, with consequent deceleration of the advancing crystalline layer (e.g., Mollo and Hammer, 2017). In the most differentiated trachyandesitic products erupted at Mt. Etna, the viscosity increase can be locally exacerbated by the late-stage formation of Fe-Ti-bearing phlogopite crystals on the walls of lava vesicles (7.9–9.2 wt% FeO and 3.7–4.5 wt% TiO_2; Nicotra et al., 2010). The removal of iron and titanium from the melt is very effective in increasing the melt viscosity (Di Genova et al., 2020; Scarani et al., 2022), especially during the decompression-induced crystallization process leading to the growth of phlogopite from Etnean magmas (Nicotra et al., 2010). Recalling the

thermodynamic principles of crystal nucleation and growth, the activation energy for crystal growth is a proxy for the enthalpy difference associated with the transport of structural units across the crystal-melt interface (Kirkpatrick, 1975). Therefore, the growth of concentric bands over a short length scale of only 15–20 μm can be mutually associated with an increase in the activation energy for crystal growth by H_2O exsolution and formation of an increased number of stronger Si—O—Si bonds relative to weaker Si—OH—HO—Si bonds (Kirkpatrick, 1975).

Changes in the growth history of a crystalline solution produce kinetically-controlled cation substitution reactions in which the excess Gibbs free energy of mixing is resolved by large enthalpic effects through distortion of the lattice (Ganguly and Saxena, 1987). In this regard, the enthalpy of mixing (ΔH_{mix}) of a solid solution is often described by two components: (1) a strain energy term arising from the mismatch in size when one cation substitutes for another of different size, and (2) a chemical energy term resulting from the interactions of the atoms with their surroundings in the crystal lattice (Ganguly and Saxena, 1987). The contribution of this latter term on ΔH_{mix} is associated either with differences in electronegativity and electronic polarization of the substituting cations, or with electronic effects accounting for the change of ligand field stabilization energy of transition metal cations as a function of the composition of the solid solution (Ganguly and Saxena, 1987). For coupled heterovalent substitutions along the join $CaMgSi_2O_6$-$CaAl_2SiO_6$, the activities of the end-member components approach their molar fractions (e.g., $a_{Di} \approx X_{Di}$ and $a_{CaTs} \approx X_{CaTs}$), despite the calorimetric and structural data suggest charge imbalance within the solid solution (Wood, 1979). Therefore, it is expected that both ΔH_{mix} and $T\Delta S_{mix}$ increase of the same magnitude during heterovalent substitutions, such that ΔG_{mix} of charge balance and imbalance configurations remains ideally the same. In concentric zoning patterns, the partitioning energetics of Cr, Ni, and Co (i.e., 3d-cations in relation to the electronic energy of orbitals) can be related to the ΔH_{mix} between Di and CaTs end-members in clinopyroxene solid solution as (Ganguly and Saxena, 1987):

$$\Delta H_{mix} = (1 - X_{CaTs})X^2_{CaTs}W_{DiCaTs} + (1 - X_{CaTs})^2X_{CaTs}W_{CaTsDi} + \Delta CFSE_{mix} \quad (1)$$

where W_{DiCaTs} and W_{CaTsDi} are the Margules mixing parameters. As the metal–oxygen bond distance decreases, the d orbital splitting energy separation Δ (i.e., crystal field splitting) of transition metals increases. Consequently, the energetic contribution of $\Delta CFSE_{mix}$ to Eq. (1) may effectively rule the thermodynamic properties of concentric bands in response to the strong repulsive forces of electrons in orbitals surrounded by negatively charged O^{2-} anions. The leverage of crystal field effects on the crystallochemical peculiarities of concentric bands is determined by the cation-oxygen distance and geometry of M1 polyhedra (Langer and Andrut, 1996), such as $D_i \approx f(\Delta CFSE_{mix})$ when $^{oct}CFSE$ attains the highest value. This observation has important ramifications for the interpretation Cr-Ni-Co-rich concentric zoning patterns in natural clinopyroxene phenocrysts and intuitively ascribed to compositionally distinct magmas that mix together under open-system crystallization conditions (e.g., Ubide and Kamber, 2018; Ubide et al., 2019a, 2019b; Di Stefano et al., 2020; Mollo et al., 2020b; Petrone et al., 2022). Cr-Ni-Co-rich clinopyroxene bands can be related to counterintuitive processes driven by the perturbed growth histories of crystals and discontinuous accumulation/depletion of cations at the crystal-melt interface. Importantly, natural sector-zoned clinopyroxene at Mt. Etna shows major element variations (Masotta et al., 2020) and rare earth element systematics (MacDonald et al., 2022) indicative of crystallization at low degrees of undercooling under sluggish kinetic effects, and therefore, concentric zoning in transition metals is a viable tool for tracking magma mixing events. Nevertheless, the overriding implication of closed-system experiments from this study is that partitioning kinetics under strong cooling and decompression regimes can be steadily convoluted with the change of crystal growth mechanisms and only subordinately controlled by simple stoichiometric mixing between mafic (Cr-Ni-Co-rich) and more differentiated (Cr-Ni-Co-poor) basaltic melts.

Strong disequilibrium effects resulting from the early imposition of CR_{mid} and CR_{fast} before melt decompression in experiments *EXP-0.01* and *EXP-1* are associated with the uptake of Cr cations in Tschermak-rich intrasectoral subsectors, together with the concurrent increase of Sc, V, and HFSE in the M1-site (Figs. 4 and 6). Cr concentrates in the crystalline layer regardless of crystal field effects, as indicated by the lack of concurrent uptake of Ni and Co in the M1-site (Fig. 6). The CD transect in Fig. 4 indicates that charge imbalance effects caused by the excess of ^{T}Al in intrasectoral subsectors are resolved through the Tschermak-type substitution $[^{T}Si, ^{M1}Mg] \leftrightarrow [^{T}Al, ^{M1}Cr]$, which involves the formation of chromium-aluminium Tschermak component $CaCrAlSiO_6$ (Duncan and Preston, 1980; Hill et al., 2000, 2011; Mollo et al., 2020a, 2020b). As a result, the energetic contribution of $\Delta CFSE_{mix}$ is overwhelmingly mediated by the rapid growth of Tschermak-rich crystalline frameworks, in which Cr cations more readily enter the M1-site of $CaAl_2SiO_6$ (3 + charge on M1) than $CaMgSi_2O_6$ (2 + charge on M1) due to charge deficit left by the replacement of ^{T}Si by ^{T}Al (Mollo et al., 2013). This extends also to the partitioning of Sc and V in M1-site, which accounts for clinopyroxene structural configurations related to the Tschermak components $CaScAlSiO_6$ and $CaVAl_2O_6$, respectively (Bennett et al., 2004; Hill et al., 2011; Mollo et al., 2020b). V populates the M1-site of clinopyroxene mainly as V^{4+} at the redox state of the experiments and natural Etnean magmas, as derived by the thermodynamic parameterization of Mallmann and O'Neill (2009) on the multivalence state of D_V as a function of fO_2. This is also confirmed by the experimental study of Toplis and Corgne (2002) showing that V^{5+} becomes the dominant valence state only at $fO_2 > NNO + 2$. When crystals grow from supersaturated melts, nucleation first occurs under high driving force conditions, which will diminish as growth proceeds. Therefore, a crystal which is originally skeletal or dendritic will eventually take a polyhedral form bounded by a flat face as melt chemical gradients decline over time via diffusive relaxation (Pontesilli et al., 2019). In the context of our experiments, skeletal and dendritic shapes correspond to an early stage of diffusion-limited growth before the attainment of a more stable crystal surface under interface-limited growth conditions. For hydrous Etnean magmas, the rapid growth of skeletal and dendritic clinopyroxene crystals has been calculated to increase up to a maximum of $\sim 10^{-5}$ cm/s by rapid cooling and decompression experiments (Simakin et al., 2003; Pontesilli et al., 2019; Arzilli et al., 2019, 2022). Partitioning data from this study suggest that the energetic contribution of $\Delta CFSE_{mix}$ on the incorporation of highly charged cations in the M1-site of sector-zoned clinopyroxene crystals is effective only upon slow growth rates, on the order of 10^{-7} cm/s. As the growth rate increases up to 10^{-5} cm/s at the early stage of cooling, the interface melt next to the advancing crystal surface becomes dramatically enriched in incompatible Al + Ti cations and depleted in compatible Si + Mg cations (Mollo et al., 2010, 2012). This enhances the substitution of cations of very different size (i.e., replacement of ^{T}Si by ^{T}Al with ionic radius of 0.26 and 0.39 Å, respectively), with consequent large enthalpic effects due to distortion of the lattice and change in the coulombic forces that mitigate the contribution of $\Delta CFSE_{mix}$ on the incorporation reaction.

As the crystal growth rate and chemical gradients in the melt diminish with annealing time, skeletal frameworks are subsequently infilled by more relaxed melts. In this late stage, the transition between diffusion-limited to interface-limited growth regime leads to the formation of polyhedral morphologies in which trace element sector partitioning takes place via the mutual substitution reaction $[DiHd]_{\{-1\,1\,1\}} \leftrightarrow [REE + YCaTs + HFSECaTs]_{\{h\ k\ 0\}}$ proposed in recent works on natural and experimental sector-zoned clinopyroxene (Ubide et al., 2019a, 2019b; Di Fiore et al., 2021; MacDonald et al., 2022). The growth rate of sector-zoned crystals must be slow to attain planar faces by filling up the interstices of earlier-formed dendrites through a layer growth

mechanism that is established at low melt saturation conditions. The structural configuration of the advancing interface determines the geometrical distribution and concentration of cations that are progressively incorporated into the early-formed crystalline surface that will eventually build the bulk crystal (Nakamura, 1973; Leung, 1974). However, nonequivalence of element partitioning between different time-equivalent faces requires that growth rates on adjacent faces differ and sector zoning depends on the sensitivity of a specific cation partitioning to growth rate. This is possible because {−1 1 1} and {*h k* 0} sectors have unique cation orientations and configurations of the growth surfaces, leading to different degrees of crystal-melt cation substitutions during growth (Nakamura, 1973; Dowty, 1976, 1977). From a crystallographic and crystallochemical point of view, sectoral partitioning in clinopyroxene depends on the two-dimensional (2D) atomic arrangements of the growing layers (Hollister and Gancarz, 1971; Ferguson, 1973; Leung, 1974) and is principally controlled by the attachment kinetics of SiO_3 chains and the adsorption/desorption kinetics of cations in the protosites, as partially-completed crystal structures that are more flexible than the future M1- and M2-sites (Nakamura, 1973; Dowty, 1976, 1977; Shimizu, 1981). Therefore, the susceptibility of a given sector to crystal-melt cation substitutions is influenced by a local 2D nearest neighbor effect, since the overall 3D nearest-neighbor coordination is essentially unchanged, except for subtle differences of bond lengths and site distortion. The protosite concept assumes local equilibrium between the crystal surface and the surrounding melt and is independent on the crystal growth mechanism (Nakamura, 1973), which is not clearly defined in literature and may change as a function of the degree of undercooling (Kouchi et al., 1983). Differential partitioning between structurally different regions of the crystal surface is controlled by the types of protosites, consisting of different coordination and geometry of cations within a growth layer (Nakamura, 1973; Leung, 1974; Dowty, 1976, 1977). Once cations are incorporated in different concentrations on nonequivalent growing sectors and then ordered under successive layers, adjustments in their concentrations are precluded by sluggish intracrystalline diffusion rates (Hollister and Gancarz, 1971; Dowty, 1976, 1977).

The {−1 1 1} sector grows along the *c*-axis and its spatial structural distribution consists of parallel planes that expose single layers of M2-protosites alternating with double layers of M1-protosites (Fig. 9a). The structural arrangement of the {−1 1 1} sector implies that a smaller number of protosites are simultaneously exposed along the planar face (Nakamura, 1973; Leung, 1974). This favors the incorporation of cations structurally important for the lattice site, by minimizing the concentration of unfavorable impurity cations (i.e., non-essential structural constituents) in the adsorption layer (Hollister and Gancarz, 1971; Nakamura, 1973; Leung, 1974; Dowty, 1976, 1977). In contrast, the {1 0 0} sector grows parallel to the *c*-axis and consists of double layers of M1-protosites and double layers of M2-protosites (Fig. 9a). Because an increased number of protosites are now exposed in the adsorption layer, a larger amount of unfavorable impurity cations can be accepted to fill this structural arrangement (Nakamura, 1973; Leung, 1974). Incorporation of impurity cations with different charge and size relative to those of the host constituent cation is facilitated by the geometrical flexibility of the protosites, whereas charge balance in the lattice occurs through the addition of a subsequent adsorption layer parallel to the crystal face (Nakamura, 1973; Leung, 1974). The activation energy for crystal growth in the system $CaMgSi_2O_6$-$CaAl_2SiO_6$ increases with increasing impurities (mainly Al and Ti) in the lattice site of clinopyroxene (Kirkpatrick, 1975), giving reason for the fast growth of Si-Mg-rich, Al-Ti-poor {−1 1 1} sectors relative the slow growth of Si-Mg-poor, Al-Ti-rich {1 0 0} sectors (Fig. 9a). Moreover, the ratio between length and width of the crystal must be constant at all growth stages to maintain the prismatic habit and shape stability (Leung, 1974). Therefore, time-equivalent sector boundaries belonging to crystallographically nonequivalent faces can retain their planar surfaces via morphological stability only if the different faces grow at constant relative velocities (Hollister and Gancarz, 1971; Ferguson, 1973; Nakamura, 1973; Leung, 1974). As summarized in Fig. 9a, there is need that L/W and $G_{\{-111\}}/G_{\{100\}}$ are constant, with $L > W$ and $G_{\{-111\}} > G_{\{100\}}$ to increase the size of the prisms along the *c*-axis.

Regarding the number and type of protosites exposed on each face per unit cell volume, four M1 3/6 protosites are exposed on the slow growing {1 0 0} sector and only one M1 4/6 protosite is exposed on the fast growing {−1 1 1} sector (where 3/6 and 4/6 are the number of bonds in the first coordination sphere crossing the crystal surface of least bonding; Nakamura, 1973; Dowty, 1976, 1977; Shimizu; 1981). The

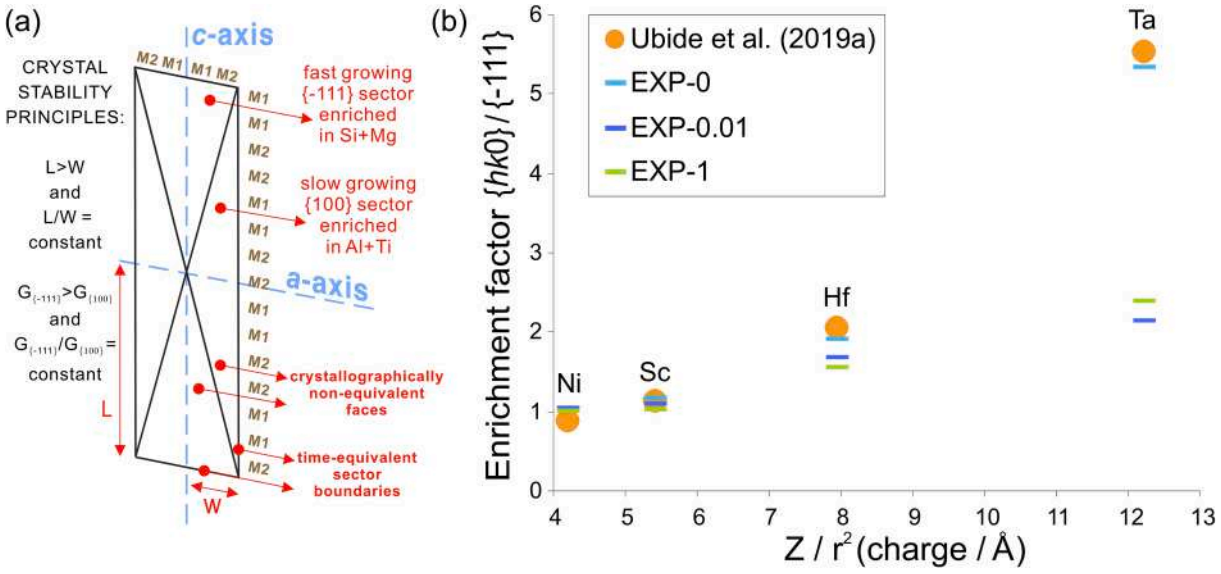

Fig. 9. Schematic illustration of crystal growth principles governing the structurally different regions of a sector-zoned clinopyroxene (a). Figure redrawn after Nakamura (1973) and Leung (1974). L, crystal length. W, crystal width. G, growth rate of {−1 1 1} and {1 1 0} sectors. Enrichment of cations in sector-zoned clinopyroxene crystals from the isobaric experiment EXP-0, slow decompression experiment EXP-0.01, and fast decompression experiment EXP-1 as a function of the ratio of the ionic charge (Z) of the cation divided by the ionic radius (r) squared (b). The enrichment factor is calculated as the ratio of an element concentration in {*h k* 0} relative to {−1 1 1} sectors, according to Shimizu (1981). Experimental enrichment factors are compared with the natural data set of Ubide et al. (2019a) obtained for phenocrysts from Mt. Etna.

higher number of protosites exposed in the slow growing {1 0 0} sector explains its greater predisposition to retain trace cations with high charge and small size relative to the fast growing {−1 1 1} sector. Shimizu (1981) outlines that the enrichment of cations is proportional to the ratio of the ionic charge of the cation divided by the ionic radius squared, as a measure of the strength of the Coulomb interaction between a given cation and the protosite. The stronger the Coulomb interaction, the higher the ionic potential, the higher the retention of cations absorbed in the M1-site. Ubide et al. (2019a) found the same relationship for titanaugite phenocrysts at Mt. Etna, and experimental crystals obtained from *EXP-0* under slow cooling and isobaric conditions compare very well with the natural data set (Fig. 9b). In contrast, growth kinetics are exacerbated in experiments *EXP-0.01* and *EXP-1* due to an increased cooling rate and the concurrent effect of melt decompression. This causes crystal morphological instability via melt chemical perturbations and change in the velocity of the sector surface (Kouchi et al., 1983). As a result, the compositional difference between basal and prism sectors decreases and the enrichment factor also decreases (Fig. 9b). This trend is especially evident for $HFSE^{4+}$ and $HFSE^{5+}$ because these elements are more susceptible to the increased proportion of structural configurations important for the accommodation of highly charged cations relative to Mg, as the major host cation in the M1-site (Mollo et al., 2018).

4.3. Lattice strain parameterization

In line with previous studies on clinopyroxene partitioning energetics (Wood and Blundy, 2001; Blundy and Wood, 2003; Brooker et al., 2003; Mollo et al., 2020b), partition coefficients for monovalent (D_{Li}, D_{Na}, D_K, D_{Rb}, and D_{Cs}; $^{M2}D^{+1}$), divalent (D_{Mg}, D_{Ca}, D_{Sr}, D_{Pb}, and D_{Ba}; $^{M2}D^{+2}$) and trivalent (D_{REE+Y}; $^{M2}D^{+3}$) cations hosted in the M2-site are investigated to extrapolate thermodynamic parameters governing the magnitude of ΔG_{strain}. These three groups include at least five partition coefficients for isovalent cations, which is a prerequisite necessary to quantitatively constrain partitioning energetics through regression analysis of data by minimizing the error of the fit. The lattice strain model of Blundy and Wood (1994) has been employed to relate $^{M2}D^{+1}$, $^{M2}D^{+2}$, and $^{M2}D^{+3}$ with the crystallochemical properties of the host crystal:

$$D_i = D_0 exp\left\{\frac{-4\pi E N_A\left[\frac{r_0}{2}(r_i - r_0)^2 + \frac{1}{3}(r_i - r_0)^3\right]}{RT}\right\} \quad (2)$$

where N_A is the Avogadro's number 6.022×10^{23} mol^{-1}, R is the universal gas constant 0.0083145 kJ/mol, and T is the temperature in Kelvin. The control of lattice strain on D_i reflects the ability of a relatively rigid crystal site to accommodate misfit trace cations with charge Z_i and ionic radius r_i (from Shannon, 1976) different to those of the host major cations normally resident on the crystallographic site. The parameter r_0 is the strain-free ionic radius and the excess of strain energy depends on insertion of cations that are bigger or smaller than the optimum radius of the site. The produced lattice strain is proportional to the apparent Young's modulus E and its effect on the curvature of the partitioning parabola (e.g., opening of the parabola limbs increases with increasing site elasticity and decreasing E). For the fictive exchange between major and trace cations, $^{M2}D^{+1}$, $^{M2}D^{+2}$, and $^{M2}D^{+3}$ are maximum at $r_i/r_0 = 1$, whereby the substituting trace cation enters the crystal lattice without strain. At this minimum energetic condition, r_0 intersects the apex of the parabola at the strain-free (or strain-compensated) partition coefficient D_0, defining the height of the curve.

Through a Levenberg–Marquardt-type, non-linear least-squares

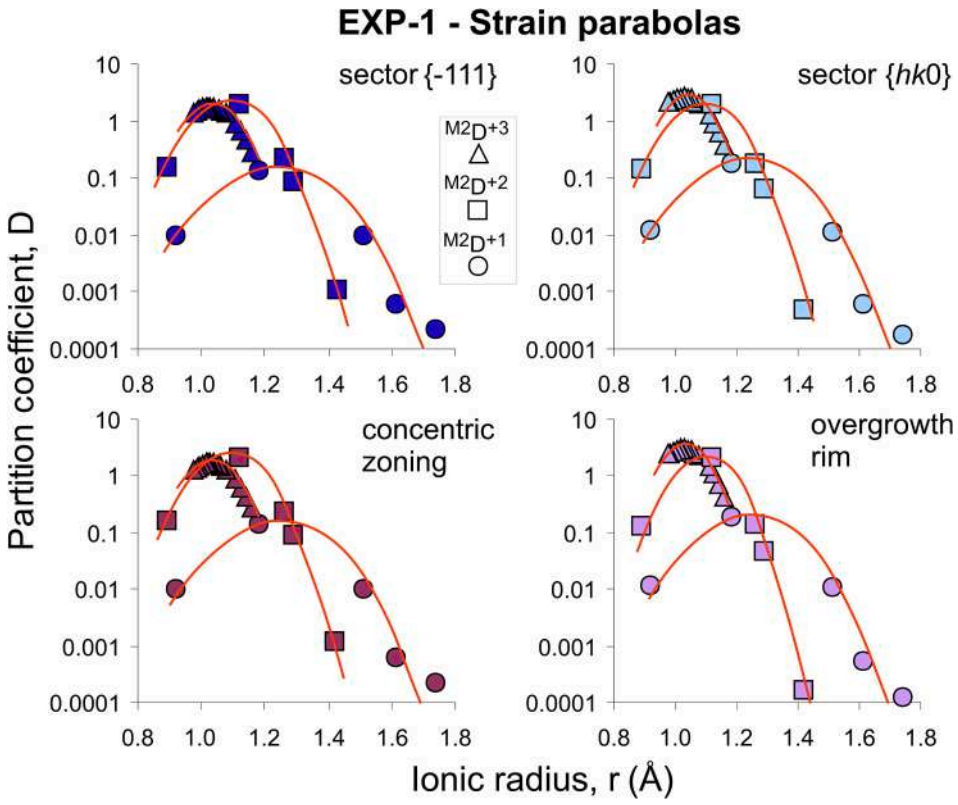

Fig. 10. Example of strain parabolas obtained for the fast decompression experiment *EXP-1*. Partition coefficients calculated for suites of isovalent cations hosted in the M2-sites of different clinopyroxene zones are plotted against the cation ionic radius (r). Most of error bars are within the symbols and are not plotted for the sake of clarity. See all plots obtained for the isobaric experiment *EXP-0*, slow decompression experiment *EXP-0.01*, and fast decompression experiment *EXP-1* in Supplementary Material 7.

fitting routine, the best-fit values of D_0, r_0, and E are derived by weighting the fits using the standard deviations of measured partition coefficients (see data in Table S6). All plots of partition coefficient against ionic radius for suites of isovalent cations from isobaric experiment *EXP-0* and decompression experiments *EXP-0.01* and *EXP-1* are presented in Fig. S2. An example is displayed in Fig. 10 for partitioning data from *EXP-1*, where values of $^{M2}D^{+1}$, $^{M2}D^{+2}$, and $^{M2}D^{+3}$ lie on parabola-like curves in accordance with the cardinal study of Onuma et al. (1968), which laid the groundwork for several predictive models reported in literature (e.g., Wood and Blundy, 1997; Sun and Liang, 2012, Beard et al., 2019; Mollo et al., 2018). Crystal solid solutions are less compressible than the more disordered and flexible structure of the melt, thus the lattice strain parameterization has the advantage of eliminating most of melt compositional effects on mineral–melt partitioning (Blundy and Wood, 1994).

Onuma curves for $^{M2}D^{+1}$, $^{M2}D^{+2}$, and $^{M2}D^{+3}$ from hourglass {−1 1 1} and prism {*h k* 0} sectors, concentric bands, and overgrowth rims are comparatively displayed in Fig. 10. Partitioning parabolas become tighter with increasing ^{T}Al and/or the cation charge for the same isovalent group, because there is a strong crystallochemical control of clinopyroxene on the excess of strain energy under both equilibrium (Wood and Blundy, 2001; Blundy and Wood, 2003) and kinetic growth (Mollo et al., 2013) conditions. The main mechanism responsible for the apparent stiffening of the lattice is related to the different ionic radius of aluminium and silicon in the T-site of clinopyroxene. Al-O bonds are longer than Si-O bonds and the replacement of ^{T}Si by ^{T}Al shortens the cation–oxygen bond distance of the M2 polyhedron by increasing the resistance of the site to local deformation (Hill et al., 2000; Mollo et al., 2020a).

It worth mentioning that all fits derived by Eq. (2) are in very good agreement with measured partition coefficients (Fig. 10 and Fig. S2), irrespective of the clinopyroxene zoning pattern examined and the experimental conditions adopted (see regression statistics in Table S6). Partition coefficients for the trace cations are approximated to within ±10% by our fits to the lattice strain model. This supports the recognition that kinetically-controlled cation substitution reactions affect $^{M2}D^{+1}$, $^{M2}D^{+2}$, and $^{M2}D^{+3}$ through charge balance mechanisms analogous to those observed during equilibrium partitioning, as outlined in Mollo et al. (2013). Kinetic incorporation of trace cations in the lattice site proceeds by the attainment of a local interface equilibrium, as small-volume reaction kinetics develop at the crystal-melt interface by a steady-state diffusive mass transport in high-temperature, low-viscosity basaltic melts (Mollo et al., 2013; Lang et al., 2021, 2022). Adherence of $^{M2}D^{+1}$, $^{M2}D^{+2}$, and $^{M2}D^{+3}$ to parabolic variations confirms the reliability of our partition coefficients, by excluding any sort of contamination due to random incorporation of small amounts of a diffusive melt and phlogopite microlites into the crystalline material during LA-ICP-MS analysis. As assessed by Kennedy et al. (1993), Lofgren et al. (2006), and Mollo et al. (2013), such trapping processes would yield partition coefficients which are independent of cation charge and radius. By simulating a very low percentage (4%) of glass and phlogopite contamination for clinopyroxene, the fictive pattern obtained for isovalent cations does not return regular Onuma relationships (see the comparative diagram in Fig. S3). In contrast, the alignment of partition coefficients from this study correlates well with partitioning parabolas examined under the rational of thermodynamic principles and determined for chemically homogeneous bulk systems under equilibrium crystallization conditions (e.g., Brooker et al., 2003).

Fig. 10 shows that $^{M2}D_0^{+3} < {}^{M2}D_0^{+2}$ for ^{T}Al-poor {−1 1 1} sectors and concentric bands analyzed under fast cooling and decompression conditions, whilst $^{M2}D_0^{+3} > {}^{M2}D_0^{+2}$ for ^{T}Al-rich {*h k* 0} sectors and overgrowth rims. This cross-over denotes that the height of the Onuma parabola is markedly controlled by the incorporation of aluminium in tetrahedral coordination and the increased probability for REE + Y to enter a locally charge-balanced site (Wood and Blundy, 2001). It is worth noting that the relation $^{M2}D_0^{+3} > {}^{M2}D_0^{+1}$ remains unchanged for all the clinopyroxene compositions (Fig. 10), attesting the negligible role of ^{M2}Na relative to ^{T}Al on the incorporation reaction of REE + Y during crystallization of basaltic magmas at low-*P* (Mollo et al., 2018). The entry of ^{M2}Na is ineffective as a charge-compensating cation because the replacement of ^{M2}Ca^{T}Al with ^{M2}Na^{T}Si is subordinate to charge imbalanced configurations resulting from the accommodation ^{T}Al in the lattice site (Adam and Green, 2006; Bennett et al., 2004). An opposite relationship of $^{M2}D_0^{+3} < {}^{M2}D_0^{+1}$ is documented only at mantle pressure in response to the small partial molar volume of jadeite and its preferential dissolution in clinopyroxene at high-*P* (Blundy and Dalton, 2000).

In Fig. 11, D_0, r_0, and E from Eq. (2) are plotted as a function of the most important crystallochemical parameters of clinopyroxene, in conjunction with an internally consistent data set reported in the review of Mollo et al. (2020b). This comparative data set refers to chemically homogeneous ^{T}Al-rich clinopyroxene crystals equilibrated with a phonotephritic melt (P = 300 MPa, T = 1150 and 1180 °C, and fO_2 = NNO + 1), using the same experimental apparatus and regression approach presented in this work. As ^{T}Al increases in clinopyroxene, values of $^{M2}E^{+1}$, $^{M2}E^{+2}$, and $^{M2}E^{+3}$ from kinetic experiments linearly increase (Fig. 11a) and, comparatively, values of $^{M2}r_0^{+1}$, $^{M2}r_0^{+2}$, and $^{M2}r_0^{+3}$ linearly decrease (Fig. 11b). These concurrent variations closely match those observed for the equilibrium partitioning data set of Mollo et al. (2020b) and extend the control of major cation configurations on the elastic property and coordination polyhedra of clinopyroxene to kinetic growth conditions. The enhanced stability of Tschermak components is accompanied by the entry of a highly charged central cation in the coordination polyhedron, which lowers the anion repulsive forces between two oxygens and produces shortening of the coordinating cation–oxygen bond distances of M1- and M2-sites (Blundy and Dalton, 2000; Blundy and Wood, 2003). Crystallochemical effects increase the resistance of the lattice site to local deformation by increasing the Young's modulus (Fig. 11a) and produce a net positive charge at the coordination polyhedron that more readily attracts the coordinating oxygen anions around the lattice site by lowering the strain-free ionic radius (Fig. 11b) (cf. Hill et al., 2000; Wood and Trigila, 2001; Dygert et al., 2014; Adam and Green, 2006; Mollo et al., 2013, 2020b; Di Fiore et al., 2021).

In Fig. 11c, $^{M2}D_0^{+1}$ and $^{M2}D_0^{+3}$ from both kinetic and equilibrium partitioning experiments depict analogous trends with increasing ^{T}Al due to the major control exercised by lattice strain energetics on the incorporation of monovalent and trivalent cations in the M2-site. $^{M2}D_0^{+2}$ from kinetic experiments is almost insensitive to ^{T}Al. In contrast, the data set of Mollo et al. (2020b) shows a marked declining trend for $^{M2}D_0^{+2}$ (Fig. 11c) because clinopyroxene crystals with lower ^{M2}Ca contents are in equilibrium with melts progressively depleted in CaO. As discussed earlier, the net charge of major divalent cations hosted in the M2-site does not change in the $CaMgSi_2O_6$-$CaAl_2SiO_6$ solid solution during the growth of complexly zoned clinopyroxene crystals. This explains why the stoichiometric amount of ^{M2}Ca in zoned crystals shows an almost negligible variation within ~2% (Table S3). Similarly, ^{M2}Ca profiles across {−1 1 1} and {*h k* 0} sectors and recharge bands of natural clinopyroxene phenocrysts at Mt. Etna are virtually flat, with no observable partitioning effects (see Fig. 3 in Ubide et al., 2019a). The constancy of ^{M2}Ca in different clinopyroxene zones is offset for the dependency of $^{M2}D_0^{+2}$ on ^{T}Al under kinetic growth conditions. It follows that larger divalent trace cations (i.e., Sr and Pb) are less favorably incorporated in the coordination polyhedron (Fig. 8), in response to the electronic polarization of the coordinating oxygen anions around the lattice site and the consequent decrease of the strain-free ionic radius (Fig. 11b).

4.4. Electrostatic parameterization

The electrostatic model developed by Wood and Blundy (2001) is complementary to the early lattice strain model proposed by the same authors (Blundy and Wood, 1994) and considers the crystal lattice as a dielectric and elastic continuum medium. While a fully charge-balanced

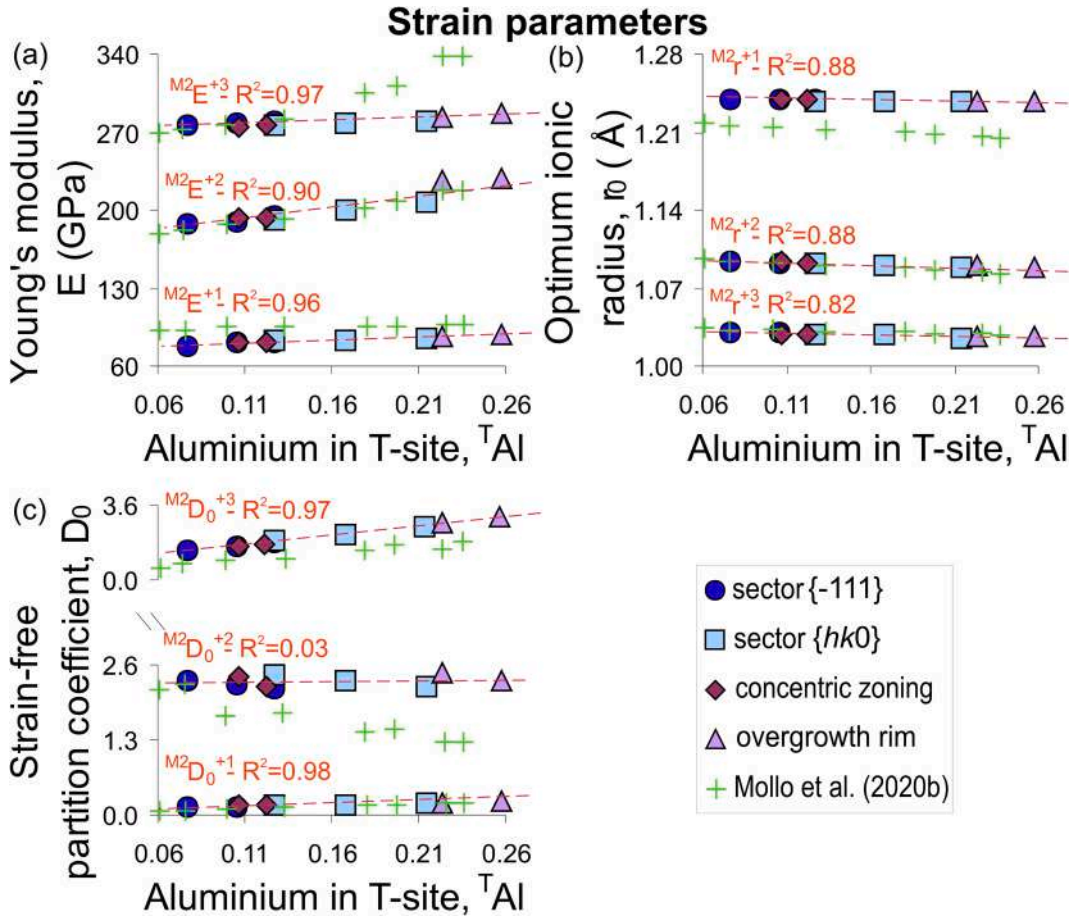

Fig. 11. Strain parameters calculated for the isobaric experiment *EXP-0*, slow decompression experiment *EXP-0.01*, and fast decompression experiment *EXP-1* are plotted against aluminium in T-site. Experimental data are aligned as described in Fig. 8. Diagrams show the Young's modulus E (a), optimum ionic radius r_0 (b), and strain-free partition coefficient D_0 (c). Most of error bars are within the symbols and are not plotted for the sake of clarity. Strain parameters from this study are compared with those reported in Mollo et al. (2020a, 2020b). See the text for details.

isovalent substitution causes only excess of lattice strain and has no electrostatic energy penalty, a charge-imbalanced heterovalent substitution requires that electrostatic work is done when a trace cation entering the lattice site without strain has charge Z_i different from that of the major resident cation Z_0 (i.e., optimum charge). Following this principle, D_0 for each isovalent group of trace elements shows a parabolic dependence on Z_i (Blundy and Wood, 2003; Wood and Blundy, 2001). When both r_i/r_0 and Z_i/Z_0 are equal to 1, the apex of the parabola corresponds to D_{00} and the substitution reaction occurs without inducing either elastic strain or electrostatic work. The electrostatic energy penalty caused by insertion of a 'wrongly' charged trace cation into a crystal lattice is proportional to the radius (ρ) of the region over which the excess charge is distributed and the dielectric constant (ε) of the undisturbed matrix lattice. The overall description of ΔG_{elec} is analogous to the parabolic relationship developed for the lattice strain model (Wood and Blundy, 2001):

$$D_i = D_{00} exp\left\{\frac{-N_A e_0^2 (Z_i - Z_0)^2}{2\varepsilon\rho RT}\right\} \quad (3)$$

where e_0 is the charge on the electron (1.6×10^{-19}C) and the electrostatic work of substitution (J mol^{-1}) is embodied in the exponential term of Eq. (3). To extend the fit of the electrostatic parabolas to four cation charges and calculate the electrostatic parameters with a reasonable low uncertainty (see data in Table S6), D_{Th} is used as a proxy for D_0^{4+} in accord with other works on the modeling of strain-free cations substituting into the M2-site of clinopyroxene (Wood and Blundy, 2001; Brooker et al., 2003; Mollo et al., 2013, 2020b). All plots of electrostatic parabolas from *EXP-0*, *EXP-0.01*, and *EXP-1* are presented in Fig. S2, and Fig. 12 shows an example of the parabolic pattern described by D_0^{1+}, D_0^{2+}, D_0^{3+}, and D_0^{4+} from *EXP-1*. The apex of each parabola moves upwards as the number of ^{T}Al cations increases in the lattice site and D_{00} is correspondingly displaced to higher values (Fig. 12). Changes in the peak position for different clinopyroxene zones reflect the variation in optimum valence of the M2-site in the $CaMgSi_2O_6$-$CaAl_2SiO_6$ solid solution (cf. Mollo et al., 2020b). Because the tightness of D_0-Z parabolas is inversely proportional to $\varepsilon\rho$, it follows that both limbs in ^{T}Al-rich {$h\,k\,0$} sectors and overgrowth rims are closer than those of ^{T}Al-poor {$-1\,1\,1$} sectors and concentric bands (Fig. 12). The curvature of electrostatic parabolas is mostly controlled by the difference between D_0^{3+} and D_0^{1+}, which progressively increases up to 117% with increasing ^{T}Al and reaches a maximum value for the overgrowth rim from *EXP-1*. The height of the electrostatic parabola depends on the marked increase of D_0^{3+} relative to D_0^{+2} and the cross-over for $D_0^{3+} > D_0^{2+}$ (Fig. 12), which is caused by fast cooling and decompression conditions as trivalent trace cations are much more easily incorporated in the crystallographic site of clinopyroxene crystals.

Fig. 13 shows the electrostatic parameters calculated for the kinetic experiments from this study in comparison with the equilibrium data set of Mollo et al. (2020b). Two opposite trends are observed for the region of electrostatic energy $\varepsilon\rho$ as a function of ^{T}Al (Fig. 13a), outlining that electrostatic effects do not operate equally throughout the crystal structure of chemically homogeneous and zoned clinopyroxene crystals. The increasing trend for the equilibrium partitioning data of Mollo et al.

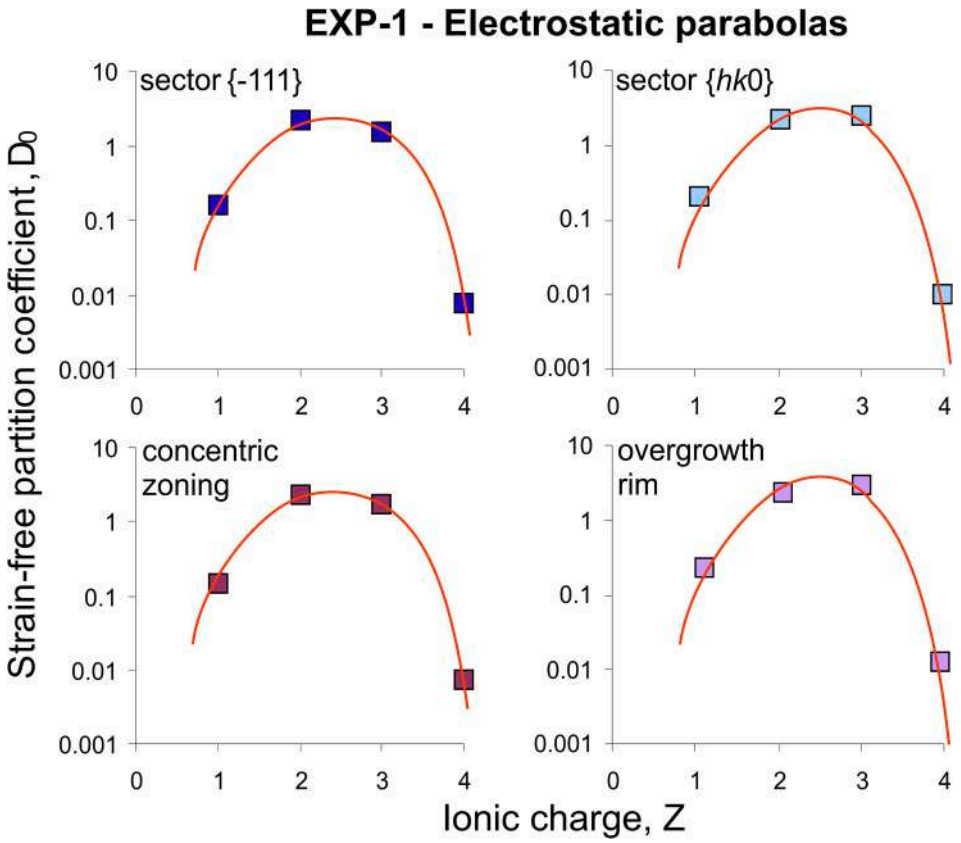

Fig. 12. Example of electrostatic parabolas obtained for the fast decompression experiment *EXP-1*. Partition coefficients calculated for divalent cations hosted in the M2-sites of different clinopyroxene zones are plotted against the cation charge (*Z*). Most of error bars are within the symbols and are not plotted for the sake of clarity. See all plots obtained for the isobaric experiment *EXP-0*, slow decompression experiment *EXP-0.01*, and fast decompression experiment *EXP-1* in Supplementary Material 7.

(2020a, 2020b) is determined by the concurrent increase of Ca and ^{T}Al in the lattice of clinopyroxene. Ca has a great polarizability (Shannon, 1993) leading to the increase of ε with increasing ^{T}Al (Fig. 13a). On the other hand, the declining trend depicted by kinetic partitioning data implies that the electrostatic energy of substitution is dominated by the concentrations of charge-balancing cations in adjacent structural sites (Fig. 13a). The dielectric constant ε represents the electrostatic response to the introduction of a material between charged particles. The lower the dielectric constant, the lower the asymmetric charge distribution in the interstitial material, the lower the induced polarization of the material caused by charge excess. Therefore, the proportion of trace cations incorporated by charge-balanced configurations increase at the expense of the proportion of charge-imbalanced configurations (Wood and Blundy, 2001; Blundy and Wood, 2003). In Fig. 13b, trends depicted by the optimum charge Z_0 concurrently increase due to the ^{T}Al-rich nature of clinopyroxene and its preference for the uptake of REE + Y cations. The larger the charge mismatch between Z_i and Z_0 (ΔZ), the smaller the partition coefficient. Focusing on the 2+ charge of Ca as the major cation hosted in the M2-site, it is calculated that ΔZ increases from 0.2 to 0.6 under both equilibrium and kinetic growth conditions, thus explaining the greater preference of ^{T}Al-rich lattice sites for the incorporation of trivalent rather than divalent trace cations. On the other hand, Fig. 13c shows contrasting trends for D_{00}, as already observed for the antithetical $\varepsilon\rho$-^{T}Al relation derived for equilibrium and chemically zoned clinopyroxene crystals (Fig. 13a). The increase of D_{00} under kinetic growth conditions denotes that the statistical proportion of M2-sites with charge −3 rather than −2 increases with increasing ^{T}Al (i.e., the negative sign indicates the effective charge on an empty structural site; Wood and Blundy, 2001; Blundy and Wood, 2003). Therefore, the average energy of heterovalent substitutions is mainly related to the concentrations of charged sites in the structure and there is a lower energy penalty to be paid for inserting trivalent trace cations in clinopyroxene with increasing D_{00}. Kinetically-induced Tschermak substitutions likely increase the ^{T}Al-^{T}Si disorder in zoned clinopyroxene crystals, thereby favoring local charge-balanced configurations, such as REE + YAl(Al$_2$)O$_6$, via the preferential formation of Al-O-Al linkages in the short-range structural arrangement of the lattice (Wood and Blundy, 2001). By viewing the crystal lattice as an isotropic dielectric medium, the proportion of charge-imbalanced configurations carrying an electrostatic energy penalty is expected to decrease because of a reduction in the overall coulombic potential energy of the M2-sites and the enhanced accommodation of trivalent cations in the lattice by charge-balanced configurations (see Section 4.5 below).

4.5. Partitioning energetic considerations

For a more comprehensive understanding of the crystal-chemical control on the partitioning of trace cations during kinetic growth conditions, it is essential to consider the electrostatic work done by placing a cation in a charge-imbalanced site and the allied electrostatic energies of substitutions resulting from the replacement of ^{T}Si for ^{T}Al (Wood and Blundy, 2001; Blundy and Wood, 2003; Hill et al., 2011; Mollo et al., 2018, 2020b). To this end, the isovalent group for REE + Y is carefully considered here, as the incorporation of these cations strictly controls the height of electrostatic parabolas (Fig. 10). Assuming for the moment that $\Delta G_{elec} = 0$ when REE + Y cations enter the M2-site of the correct −3 charge by a fully charge-balanced substitution, the thermodynamic equilibrium constant K_{ex}^{3+} for the exchange reaction of trivalent cations between clinopyroxene and melt is given by:

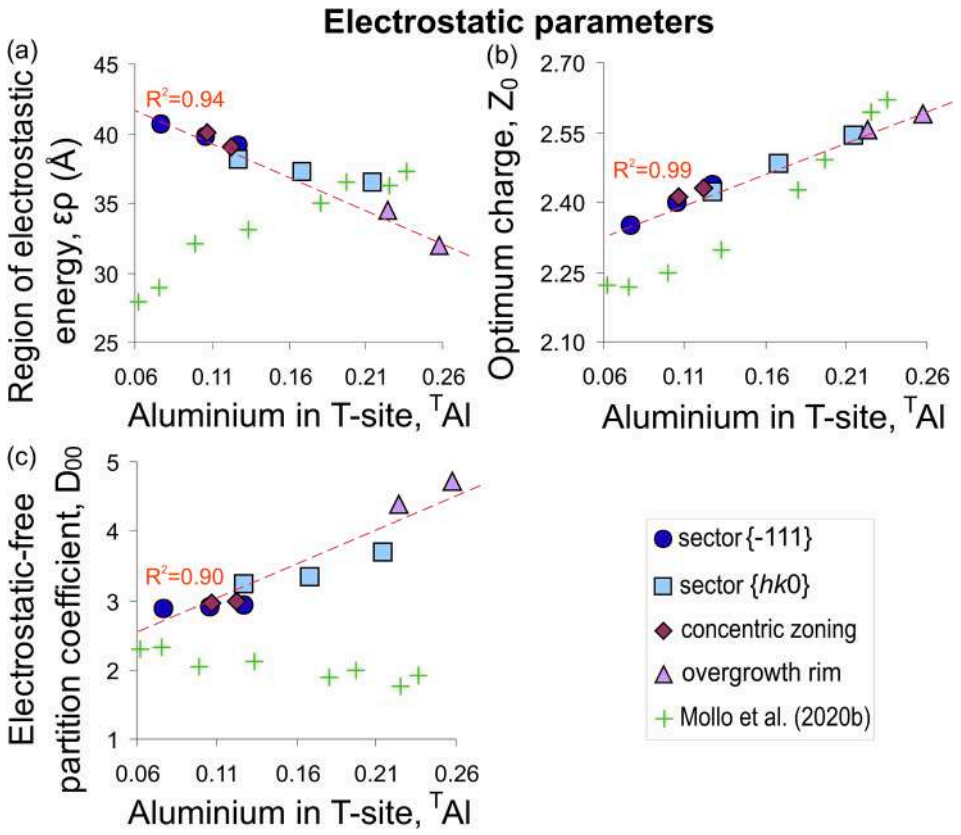

Fig. 13. Electrostatic parameters calculated for the isobaric experiment *EXP-0*, slow decompression experiment *EXP-0.01*, and fast decompression experiment *EXP-1* are plotted against aluminium in T-site. Experimental data are aligned as described in Fig. 8. The diagrams show the region of electrostatic energy $\varepsilon\rho$ (a), optimum charge Z_0 (b), and electrostatic-free partition coefficient D_{00} (c). Most of error bars are within the symbols and are not plotted for the sake of clarity. Electrostatic parameters from this study are compared with those reported in Mollo et al. (2020a, 2020b). See the text for details.

$$K_{ex}^{3+} = \frac{a^{cpx}}{a_{melt}} = \frac{[REE+Y]^{cpx}}{[X]^{3+}[REE+Y]^{melt}} \quad (4)$$

where $[X]^{3+}$ (see Table S6 for the equation) corresponds to the proportion of lattice sites charge-balanced by a cation of + 3 charge, as calculated in Wood and Blundy (2001). The activities of REE + Y in clinopyroxene and melt are approximated to the molar concentration of trace elements as $a^{cpx} = [REE+Y]^{cpx}/[X]^{3+}$ and $a^{melt} = [REE+Y]^{melt}$, respectively. By rearranging Eq. (4), we obtain that ${}^{M2}D_0^{+3}$ is:

$${}^{M2}D_0^{+3} = K_{ex}^{3+}[X]^{3+} \quad (5)$$

At the same time, however, heterovalent Tschermak substitutions require that REE + Y cations may also concentrate on M2-sites of unbalanced 'wrong' charges (i.e., 0, −1, −2, and −4). According to the electrostatic model of Wood and Blundy (2001), the probabilities of the different charged configurations can be expressed as $[X]^{0+}$, $[X]^{1+}$, $[X]^{2+}$, and $[X]^{4+}$ (see Table S6 for the equations), so that the total concentration of REE + Y in clinopyroxene contains a term for each type of M2-site multiplied by the relative probability of a REE + Y cation occupying that type of site. This thermodynamic quantity is expressed as ϕ and represents the electrostatic work done on transferring one mole of REE + Y from silicate melt to the M2-site of clinopyroxene through charge-balanced and -imbalanced configurations:

$${}^{M2}D_0^{+3} = K_{ex}^{3+}\left\{ \begin{array}{l} [X]^{3+} + \left([X]^{2+} + [X]^{4+}\right)e^{\left(\frac{-\Delta G_{elec}}{RT}\right)} \\ +[X]^{1+}e^{\left(\frac{-4\Delta G_{elec}}{RT}\right)} + [X]^{0+}e^{\left(\frac{-9\Delta G_{elec}}{RT}\right)} \end{array} \right\} = K_{ex}^{3+}\phi \quad (6)$$

Unlike for the isovalent substituents, the energy released as the ions move to accommodate a trace cation of different charge in clinopyroxene must be always greater than zero due to the polarization of the lattice (Purton et al., 1997). Regression analysis of ${}^{M2}D_0^{+3}$ against ϕ for zoned clinopyroxene crystals yields ΔG_{elec} of 32 kJ (Fig. 14a), which is close to the value of 28 kJ derived for equilibrium partitioning data (Wood and Blundy, 2001; Mollo et al. 2018, 2020b). Notably, the amount of tetrahedrally-coordinated aluminium cations in clinopyroxene from kinetic (^{T}Al = 0.08–0.26 apfu) and equilibrium (^{T}Al = 0.03–0.23 apfu) experiments varies within the same range, suggesting the effect of analogous electrostatic compensation forces when the surplus energy is distributed through the lattice of compositionally similar crystals.

The interdependence between ${}^{M2}D_0^{+3}$ and ϕ displayed in Fig. 14a is not only a proxy for the relaxation energy for charged defects but also a direct consequence of crystal structural effects related to the shortening of the M1-O distance via the coupled substitution [^{T}Si, ^{M1}Mg] ↔ [^{T}Al, ^{M1}Al] (Mollo et al., 2020b). The structural term V_c/V_{M1} has been quantified through a structural energy model where V_c and V_{M1} are the unit-cell and M1-site volumes, respectively (see Ottonello et al., 1992 for further details). It follows from Fig. 14b that an increasing solution of Tschermak components in clinopyroxene leads to the expansion of V_c and contraction of V_{M1}, with consequent distortion of clinopyroxene polyhedra due to heterovalent substitutions. As a result, ϕ (Fig. 14a) and V_c/V_{M1} (Fig. 14b) concurrently increase with increasing ${}^{M2}D_0^{+3}$, proving that the leverage of any crystallographic effect in clinopyroxene is thoroughly embodied in the proportion of charge-balanced and -imbalanced configurations (cf. Mollo et al. 2020b).

Apart from the above considerations, it is worth mentioning that the effect of melt chemistry cannot be entirely deconvoluted from the

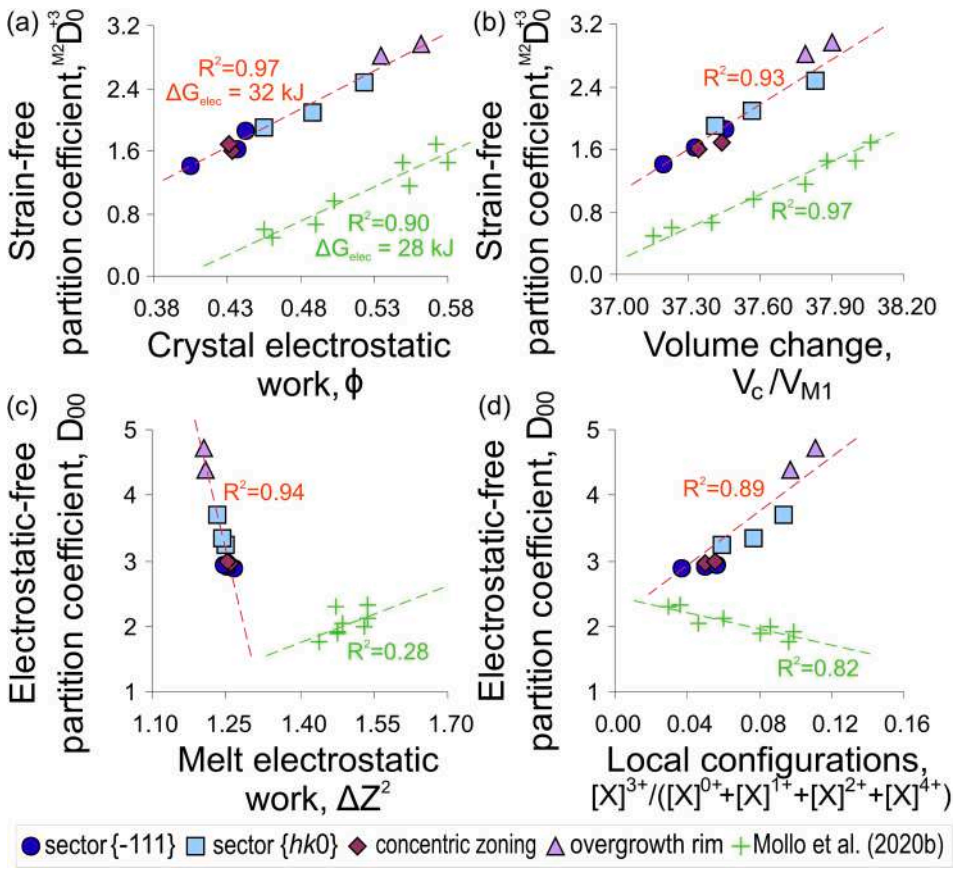

Fig. 14. Strain-free partition coefficients $^{M2}D_0^{+3}$ calculated for the isobaric experiment *EXP-0*, slow decompression experiment *EXP-0.01*, and fast decompression experiment *EXP-1* are plotted against the crystal electrostatic work ϕ (a) and the crystal volume change V_c/V_{M1} (b). Electrostatic-free partition coefficients D_{00} calculated for the isobaric experiment *EXP-0*, slow decompression experiment *EXP-0.01*, and fast decompression experiment *EXP-1* are plotted against the melt electrostatic work ΔZ^2 (c) and the configurational term $[X]^{3+}/([X]^{0+}+[X]^{1+}+[X]^{2+}+[X]^{4+})$ (d). Most of error bars are within the symbols and are not plotted for the sake of clarity. Strain and electrostatic parameters from this study are compared with those reported in Mollo et al. (2020a, 2020b). See the text for details.

structural change of the crystal lattice (Gaetani, 2004; Huang et al., 2006; Schmidt et al., 2006; Qian et al., 2015; Bonechi et al., 2021). The partitioning of REE + Y is mainly controlled by the structural arrangements of silicic melts with $NBO/T < 0.49$ (Gaetani, 2004; Huang et al., 2006), whilst the basaltic diffusive melt from this study does not differentiate towards silicic compositions and the interface melt next to the crystal surface shows little NBO/T variations on the order of 1.34–1.55 (see Section 3.5). By incorporating this structural parameter in the activity of REE + Y in the melt as $a^{melt} = [REE + Y]^{melt}/NBO/T$ (e.g., Mollo et al., 2016, 2018), it follows that Eq. (6) can be reformulated as:

$$^{M2}D_0^{+3} = K_{ex}^{3+}\frac{\phi}{NBO/T} \tag{7}$$

Regression analysis of our kinetic partitioning data indicates that the NBO/T parameter is thermodynamically implausible for the description of subtle melt changes and no statistically significant correlation is found between $^{M2}D_0^{+3}$ and the activity term $\frac{\phi}{NBO/T}$ ($R^2 = 0.00$ in Fig. S4). The thermodynamic treatment of Schmidt et al. (2006) confirms that a regular solution model for the effect NBO/T on REE + Y partitioning can be successfully formulated only over a broad melt compositional change, such as the gabbroic-granitic transition. The same conclusion has been reached for the modeling of $^{M2}D_0^{+3}$ between clinopyroxene/orthopyroxene and depolymerized picritic/basaltic melts (Sun and Liang, 2012, 2013; Yao et al., 2012).

Even though the NBO/T parameter is not a perfect descriptor for the structural configurations critically important to accommodating REE + Y in basaltic melts (cf. Bennett et al., 2004), the electrostatic work done on placing a trace cation in the melt can be parameterized by calculating the average melt-charge Z_0 as:

$$Z_0 = \frac{\Sigma\left(X_{cation}^{melt} \times charge\right)^2}{\Sigma charges} \tag{8}$$

where Al^{3+} and Si^{4+} are excluded from the calculation according to Hill et al. (2011). The activity of REE + Y in the melt is now $[REE + Y]^{melt}/\Delta Z^2$ and Eq. (6) can be reformulated as:

$$^{M2}D_0^{+3} = K_{ex}^{3+}\frac{\phi}{\Delta Z^2} \tag{9}$$

Because $^{M2}D_0^{+3}$ is tightly correlated to the activity term $\frac{\phi}{\Delta Z^2}$ ($R^2 = 0.98$ in Fig. S4), the magnitude of the electrostatic force between two charged cations in the melt serves as a rigorous descriptor for the thermodynamic partitioning reaction of REE + Y. More importantly, D_{00} linearly decreases with increasing ΔZ^2 (Fig. 14c), as the number of highly charged cations in the interface melt increases with increasing cooling and decompression rates. This applies well only to diffusive melts from this study and no statistically significant correlation between D_{00} and ΔZ^2 is calculated for the equilibrium melts derived by Mollo et al. (2020b) (Fig. 14c). From the review of Zhang (2010) on diffusion data in silicate melts, diffusion requires a species to detach from the original site, meaning breaking the bonds between the species and surrounding particles, and then move from the old site to a new site. For highly charged cations (i.e., +3, +4, and +5 charges), which are bonded strongly to other species, the detaching is rate determining for the diffusivity. In contrast, low charged cations (i.e., +1 and +2 charges) with weaker

bonds detach more easily and diffuse more rapidly (Zhang, 2010). As the crystal growth rate increases upon the effect of cooling and decompression, fast-diffusing cations with low charges are more easily rejected away from the advancing crystal surface to return to homogeneous concentration in the diffusive melt, whilst slow-diffusing cations with high charges concentrate in the interface melt feeding crystal growth (cf. Mollo and Hammer, 2017). Therefore, the electrostatic work on the melt contributes to a substantial degree on the partitioning energetics of REE + Y and their incorporation in chemically zoned crystals. Using the standardized regression coefficient (*SRC*) method described in Mollo et al. (2018), it is found that the influence (*I*) exerted by ΔZ^2 on D_{00} ($SRC_{\Delta Z2} = 0.97$ and $I_{\Delta Z2} = 51\%$) is comparable to that measured for the control of ϕ on D_{00} ($SRC_{\phi} = 0.95$ and $I_{\phi} = 49\%$). In contrast, the electrostatic work on the melt ($SRC_{\Delta Z2} = 0.53$ and $I_{\Delta Z2} = 64\%$) is subordinate to the electrostatic work on the crystal ($SRC_{\phi} = 0.95$ and $I_{\phi} = 36\%$) for the equilibrium data set of Mollo et al. (2020b).

To untangle the effects of charge-balanced and -imbalanced configurations on the incorporation of REE + Y in the M2-site and clarify the opposite D_{00}-^{T}Al trends displayed in Fig. 13c for equilibrium and kinetic growth conditions, the configurational term $[X]^{3+}/([X]^{0+}+[X]^{1+}+[X]^{2+}+[X]^{4+})$ is considered. This term describes how the proportion of charge-balanced (i.e., the concentration of REE + Y on sites of correct charges −3) and -imbalanced (i.e., the concentration of REE + Y on sites of wrong charges 0, −1, −2, and −4) configurations change in the lattice site of clinopyroxene. In Fig. 14d, values of D_{00} are plotted against $[X]^{3+}/([X]^{0+}+[X]^{1+}+[X]^{2+}+[X]^{4+})$ showing once again two contrasting trajectories. For complexly zoned clinopyroxene crystals from this study, D_{00} is observed to increase with increasing the likelihood of charge-balanced configurations relative to that of charge-imbalanced ones (Fig. 14d). Moreover, by comparing the diagrams in Fig. 14c and Fig. 14d, it is apparent that the lower the electrostatic work on the melt, the higher the number of charge-balanced configurations that may locally occur in the clinopyroxene structure as REE + YAl $(Al)_2O_6$ (cf. Wood and Blundy, 2001). This comparison legitimates the supposition that most of the electrostatic energy through the lattice of zoned clinopyroxene crystals is mediated by the average melt-charge and the electrostatic forces acting among cations distributed in the diffusive boundary layer. A supposition confirmed also by the weak influence that ΔZ^2 exercises on D_{00} derived from equilibrium partitioning data of Mollo et al. (2020b) (Fig. 14c). Under equilibrium growth conditions, the number of charge-balanced configurations is independent of the average melt-charge and may straightforwardly decrease relative to the energetics of the various charge-imbalanced configurations by lowering the magnitude of the electrostatic charging D_{00} (Fig. 14d) as ^{T}Al replaces for ^{T}Si (Fig. 13c).

4.6. Implications to magma dynamics

In their review study, Wood and Blundy (2014) emphasize that the geochemical evolution of magma (e.g., fractional crystallization) was generally modeled in the past by assuming the crystal-melt partition coefficient to be constant and independent of the *P-T-X* conditions at which crystals formed. This crude approximation resulted from either the lack of appropriate experimental data or the simplest solutions for the differential equations describing magma differentiation and related processes. For the crystallization of clinopyroxene upon variable magmatic conditions, several partitioning models specific to REE + Y have been developed in relation to the assumption of bulk thermodynamic equilibrium (i.e., conventional Berthelot-Nernst partition coefficients) and the application of lattice strain principles (Wood and Blundy, 1997; Sun and Liang, 2012; Mollo et al., 2018; Beard et al., 2019). However, in situations where trace element abundance variations are large in zoned clinopyroxene crystals, the use of models restricted to only REE + Y and based on bulk thermodynamic equilibrium may limit the possible ways in which magma differentiation processes can be investigated.

In this perspective, natural clinopyroxene phenocrysts from Mt. Etna show complex zoning patterns determined by the different physicochemical conditions encountered by magmas within a highly dynamic plumbing system, in which mafic recharge magmas rising from depth are injected into more differentiated reservoirs (e.g., Corsaro et al., 2009; Kahl et al., 2011; Ubide and Kamber, 2018). Thermodynamic calculations of Armienti et al. (2013) and Mollo et al. (2015, 2018) pointed out that the crystallization of clinopyroxene controls most of the concentration of REE + Y, HFSE, TE, and other trace elements during the geochemical evolution of Etnean magmas from the Moho transition zone to the shallowest part of the volcanic conduit, and experimental partition coefficients of the REE + Y showed magma evolution at the volcano is controlled by clinopyroxene crystallization at low degrees of undercooling (MacDonald et al., 2022). The stability field and weight fraction of clinopyroxene are much greater than those of olivine, whereas plagioclase and titanomagnetite crystallization takes place only at shallow crustal levels upon the effect of abundant decompression-driven volatile exsolution (e.g., Armienti et al., 2013; Mollo et al., 2015, 2018).

In the period from January 2011 to April 2013, several sequences of intermittent paroxysmal eruptions occurred at the newly-formed summit crater of Mt. Etna, named New South East Crater (NSEC). Cyclic fountaining activity was triggered by the arrival of hotter and volatile-rich magmas into the multi-level central conduit (Viccaro et al., 2015; Giuffrida and Viccaro, 2017; Giacomoni et al., 2018). The fractional crystallization of clinopyroxene was punctuated by replenishment events at pre-eruptive conditions of $P \approx 210$–260 MPa, $T \approx 1070$–1080 °C, and $H_2O_{dissolved} \approx 2.2$–$2.4$ wt% (Mollo et al., 2015; Moschini et al., 2021). Clinopyroxene phenocrysts are markedly zoned (i.e., $TiO_2 \approx 1$–3 wt%, $Al_2O_3 \approx 3$–9 wt%, and MgO ≈ 11–15 wt%; data from Giacomoni et al., 2018), whereas erupted bulk rocks have relatively differentiated trachybasaltic compositions (i.e., $SiO_2 \approx 47$–49 wt %, MgO ≈ 4–6 wt%, and $Na_2O + K_2O \approx 5$–7 wt%; data from Viccaro et al., 2015). For these bulk rocks, Fig. 15 shows that the concentration of La plotted against TiO_2, Sc, Th, Co, and Eu depicts distinct evolutionary paths as a function of the compatibility/incompatibility of the element of interest relative to the fractionation of clinopyroxene, except for disequilibrium overgrowth rims.

The Rayleigh fractional crystallization model is employed to quantitatively assess the role played by kinetic partitioning between clinopyroxene and melt on the trace element signature of 2011–2013 magmas:

$$C_l = C_0 F^{(D_i - 1)} \tag{10}$$

where C_l is the trace element concentration in the residual melt, C_0 is the concentration in the starting composition, and F is the fraction of melt remaining. The value of D_i corresponds to partition coefficients determined for {−1 1 1} and {*h k* 0} sectors and overgrowth rims from all of our experiments (isobaric experiment *EXP-0* and decompression experiments *EXP-0.01* and *EXP-1*). Stepwise calculations are performed by varying the mass fraction of clinopyroxene from 2% to 28%. The starting composition used for these calculations corresponds to the bulk rock analysis of a primitive magma erupted in 2002, which is suggested as the progenitor of the post-1971 eruptions at Mt. Etna on the basis of major-trace elements and Sr-Nd isotopes (Corsaro et al., 2009). Modeled fractional crystallization vectors are compared in Fig. 15 with the bulk rocks of natural rock samples. Partition coefficients calculated for {−1 1 1} and {*h k* 0} sectors capture very well the geochemical variability of 2011–2013 eruptions by fractionating a relatively low mass of clinopyroxene, whereas fractional crystallization vectors obtained for the overgrowth rims do not match with the natural compositions (Fig. 15). Perhaps the partitioning data set retrieved from clinopyroxene rims is more suitable for modeling groundmass glasses quenched at the *syn*-eruptive stage under strong saturation conditions, such as those driving the rapid growth of clinopyroxene and plagioclase microlites within the uppermost segment of the volcanic conduit. Although no

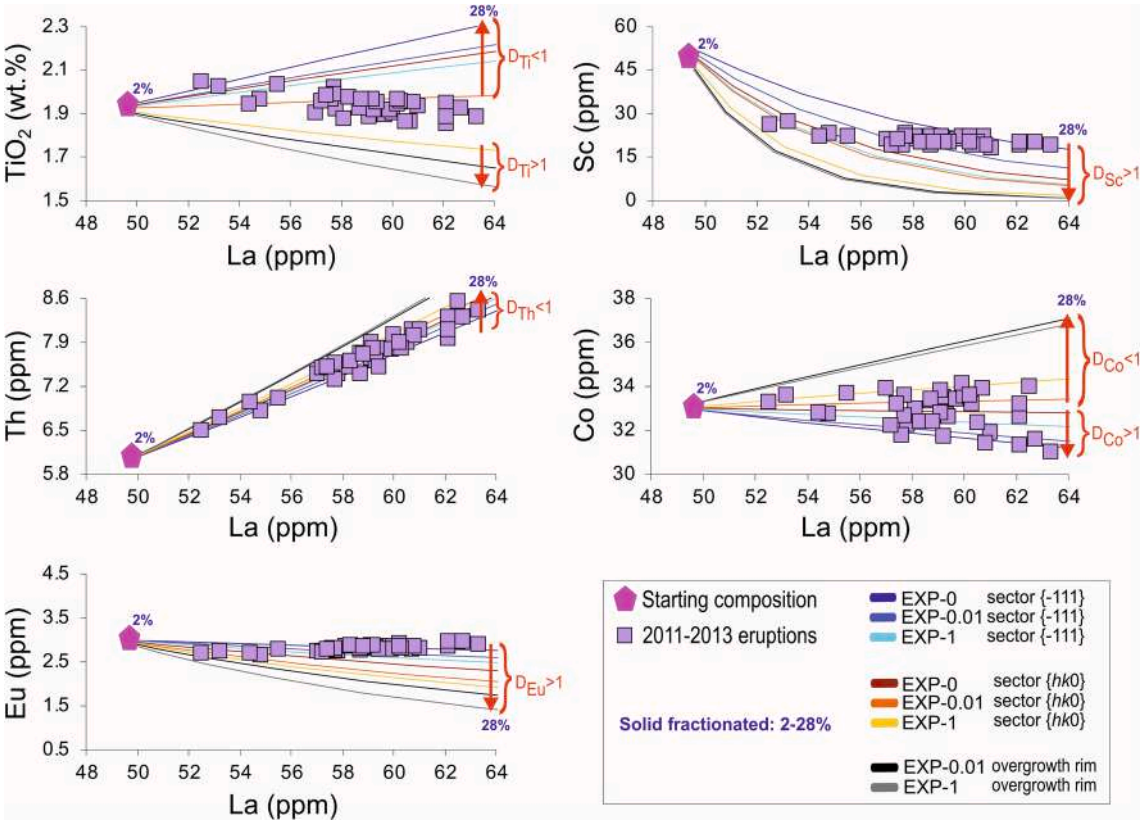

Fig. 15. Compositional evolution of bulk rock data from 2011 to 2013 eruptions at Mt. Etna. The concentration of La is plotted against TiO_2, Sc, Th, Co, and Eu. Fractional crystallization vectors obtained from the application of Rayleigh fractional crystallization equation are also plotted in figure as straight lines. Partition coefficients determined for {−1 1 1} and {*h k* 0} sectors and overgrowth rims from all of our experiments are used for the modeling. A primitive magma erupted in 2002 is selected as putative starting composition (cf. Corsaro et al., 2009). Stepwise calculations are performed by varying the mass fraction of clinopyroxene from 2% to 28%.

trace element concentrations are available in literature for 2011–2013 groundmass glasses to investigate the final step of melt solidification, it results from Fig. 15 that the evolutionary history of magmas is very complex and their trace element inventory cannot be expressed with a single equilibrium partition coefficient (cf. Marks et al., 2004). This argument extends also to the experimental values of D_{Eu} derived for {−1 1 1} and {*h k* 0} sectors that reproduce quite well the concentration of Eu in Etnean magmas. The variation of D_{Eu} in response to the effect of fO_2 on the relative proportions of Eu^{2+} and Eu^{3+} in the melt phase has been investigated for both terrestrial and extraterrestrial basaltic systems (Shearer et al., 2006 and references therein). However, the applicability of D_{Eu} as an oxygenbarometer is settled by a range of magmatic and mineralogical variables, including clinopyroxene and melt compositions, crystallization sequence, and crystallization kinetics. In particular, Shearer et al. (2006) outline that the coupled substitution [^{T}Si, ^{M2}Ca] ↔ [^{T}Al, ^{M2}REE + Y] accommodates REE + Y in clinopyroxene at the expense of Eu^{2+}. According to these authors, the growth rate and site configuration of clinopyroxene growth surfaces have a control on the fractionation of Eu^{2+} from Eu^{3+} in the lattice site, especially for depolymerized basaltic melts. Therefore, the influence of fO_2 on Eu incorporation in clinopyroxene must be placed within a crystallochemical context, in accord with the finding that a range of D_{Eu} values is required to successfully model the intrinsic variability of Eu concentrations in 2011–2013 magmas (Fig. 15). It follows that complementary kinetic effects due to cooling and decompression regimes may deeply affect the partitioning energetics of cation substitutions by changing the sign and magnitude of fractional crystallization vectors. Differently from what occurs upon the effect of a linear cooling rate where kinetic effects are insufficient to change the ability of a trace cation to be compatible or incompatible within the lattice site of clinopyroxene (cf. Mollo et al., 2013), the new experimental data set presented here shows that combined cooling and decompression regimes may change the compatibility of one cation (i.e., $D_{Ti} > 1$ against $D_{Co} < 1$) relative to another (i.e., $D_{Ti} < 1$ against $D_{Co} > 1$) for the different zones of clinopyroxene crystals (Fig. 15). This leads to the conclusion that the intracrystalline behavior of trace elements in zoned clinopyroxene phenocrysts is mainly governed by equilibrium-limiting kinetic effects due to sequences of magma cooling and decompression. Kinetics of trace element partitioning reflect local equilibrium concentrations between the surface of the growing crystal and the coexisting melt but not the bulk thermodynamic equilibrium of the solidifying system. Equilibrium thermodynamics always stresses the search for absolute energy minima when the degree of supersaturation is zero (i.e., no chemical concentration gradients) and the steady-state melt concentration at the crystal surface approaches the relaxed far-field melt composition. In chemically and physically dynamic subvolcanic environments, however, the application of this archetypal theorem is unlikely for the formation of phenocrysts characterized by composite growth histories. Also clear from Fig. 15 is that the kinetics of trace element partitioning should be considered for a more comprehensive understanding of the compositional evolution of magmas across subvolcanic systems, especially when textural complexities and intracrystalline heterogeneities are susceptive to polybaric-polythermal crystallization regimes.

5. Concluding remarks

An olivine basalt from Mt. Etna (Italy) has been variably cooled and decompressed in laboratory to investigate the kinetic control of supersaturation and diffusive relaxation on the partitioning of cations between complex zoning patterns in clinopyroxene and the adjacent melt.

The crystal morphology evolves from skeletal to hopper to polyhedral due to changes in the growth conditions, from diffusion-limited to interface-limited crystallization regimes. By combining cooling and decompression stages, experimental clinopyroxene crystals attain a composite growth history with textural attributes similar to those documented for zoned phenocrysts originating in dynamic subvolcanic systems (e.g., sector zoning, patchy zoning, and concentric zoning). Apparent partition coefficients calculated for rare earth elements and high field strength elements indicate that cation incorporation reactions can be rationalized by the complementary contribution of lattice strain and electrostatic energies of substitutions. These two thermodynamic quantities control the type and number of charge-balanced and -imbalanced configurations available to accommodate trace cations in different clinopyroxene zones. The thermodynamic description of trace cation incorporation requires that reaction kinetics at the crystal-melt interface are energetically more favored by (1) charge neutralization as silicon is replaced by aluminium in tetrahedral coordination (2) crystal volume changes via heterovalent cation substitutions, and (3) the electrostatic work done on transferring the trace cations from melt to the crystal site. The incorporation of transition metal cations into the lattice site of clinopyroxene is also ascribed to changes in the growth velocity of the advancing crystalline layer due to the mutual effects of cooling and decompression. This causes that the excess enthalpy of mixing along the join $CaMgSi_2O_6$-$CaAl_2SiO_6$ becomes a function of the crystal field stabilization energy of transition metal cations in octahedral coordination, leading to substantial Cr, Ni, and Co enrichments in the crystalline layer. The range of apparent partition coefficients from this study are used to quantitatively assess the role played by clinopyroxene fractionation on the trace element pattern of magmas erupted at Mt. Etna. Modeling results outline that the trace element signature of Etnean magmas is intrinsically related to the kinetic aspects of crystal growth.

Declaration of Competing Interest

The authors declare that they have no known competing financial interests or personal relationships that could have appeared to influence the work reported in this paper.

Acknowledgments

Two anonymous reviewers are thanked for their thoughtful comments that materially improved the presentation and discussion of our results. We are grateful to Rajdeep Dasgupta for his helpful guidance as Associate Editor. Jeffrey Catalano is also acknowledged for his editorial work as Executive Editor of Geochimica et Cosmochimica Acta. Part of this work was supported by "INGV Progetti Ricerca Libera 2021 (Grant #214/2021)" to MN and VM, "Piano di Sostegno alla Ricerca 2022 per finanziamenti a progetti di ricerca Curiosity-driven (F-CUR_CREAMI)" to FV, and "MIUR-PRIN 2022 PROVES Project (Grant #2022N4FBAA)" to SM. DDG acknowledges the funding from the European Research Council (ERC) under the European Union's Horizon Europe research and innovation programme (NANOVOLC, ERC Consolidator Grant – No. 101044772). NM acknowledges the DFG for funding of the FIB facility (grant INST 91/315-1 FUGG) and the TEM facility (grant INST 91/251-1 FUGG).

Appendix A. Supplementary material

The data of the starting melt composition, clinopyroxene and glass chemical analyses, partition coefficients, lattice strain and electrostatic parameters for *EXP-0*, *EXP-0.01*, and *EXP-1* are provided as part of the Supplementary Material. Composite zoning patterns of two representative clinopyroxene crystals from *EXP-1* and simulations of the effect of melt and phlogopite contamination on the clinopyroxene-melt partitioning parabolas are illustrated. Thermodynamic fitting of strain-free partition coefficients as a function of melt structure and melt electrostatic work are given. Supplementary material to this article can be found online at https://doi.org/10.1016/j.gca.2023.10.012.

References

Adam, J., Green, T.H., 1994. The effects of pressure and temperature on the partitioning of Ti, Sr and REE between amphibole, clinopyroxene and basaltic melts. Chem. Geol. 117, 219–233.
Adam, J., Green, T., 2006. Trace element partitioning between mica- and amphibole-bearing garnet lherzolite and hydrous melt: 1. Experimental results and the investigation of controls on partitioning behaviour. Contrib. Miner. Petrol. 152, 1–17.
Akasaka, M., Takasu, Y., Handa, M., Nagashima, M., Hamada, M., Ejima, T., 2019. Distribution of Cr^{3+} between octahedral and tetrahedral sites in synthetic blue and green $(CaMgSi_2O_6)_{95}(CaCrAlSiO_6)_5$ diopsides. Mineral. Mag. 83, 497–505.
Albarede, F., Bottinga, Y., 1972. Kinetic disequilibrium in trace element partitioning between phenocrysts and host lava. Geochim. Cosmochim. Acta 36, 141–156.
Aloisi, M., Bonaccorso, A., Gambino, S., 2006. Imaging composite dike propagation (Etna, 2002 case). J. Geophys. Res. 111.
Armienti, P., Tonarini, S., Innocenti, F., Orazio, D.M., 2007. Mount Etna pyroxene as tracer of petrogenetic processes and dynamics of the feeding system. Cenozoic Volcanism Mediterranean. Geol. Soc. Am. Special Pap. 418, 265.
Armienti, P., Perinelli, C., Putirka, K.D., 2013. A New Model to Estimate Deep-level Magma Ascent Rates, with Applications to Mt. Etna (Sicily, Italy). J. Petrol. 54, 795–813.
Arzilli, F., La Spina, G., Burton, M.R., Polacci, M., Le Gall, N., Hartley, M.E., Di Genova, D., Cai, B., Vo, N.T., Bamber, E.C., Nonni, S., Atwood, R., Llewellin, E.W., Brooker, R.A., Mader, H.M., Lee, P.D., 2019. Magma fragmentation in highly explosive basaltic eruptions induced by rapid crystallization. Nat. Geosci. 12, 1023–1028.
Arzilli, F., Polacci, M., La Spina, G., Le Gall, N., Llewellin, E.W., Brooker, R.A., Torres-Orozco, R., Di Genova, D., Neave, D.A., Hartley, M.E., Mader, H.M., Giordano, D., Atwood, R., Lee, P.D., Heidelbach, F., Burton, M.R., 2022. Dendritic crystallization in hydrous basaltic magmas controls magma mobility within the Earth's crust. Nat. Commun. 13, 3354.
Baker, D.R., 2008. The fidelity of melt inclusions as records of melt composition. Contrib. Miner. Petrol. 156, 377–395.
Beard, C.D., van Hinsberg, V.J., Stix, J., Wilke, M., 2019. Clinopyroxene/melt trace element partitioning in sodic alkaline magmas. J. Petrol. 60, 1797–1823.
Beattie, P., 1993. Olivine-melt and orthopyroxene-melt equilibria. Contrib. Miner. Petrol. 115, 103–111.
Bennett, S.L., Blundy, J., Elliott, T., 2004. The effect of sodium and titanium on crystal-melt partitioning of trace elements. Geochim. Cosmochim. Acta 68, 2335–2347.
Blundy, J.D., Cashman, K., 2005. Rapid decompression-driven crystallization recorded by melt inclusions from Mount St. Helens volcano. Geology 33 (10), 793–796.
Blundy, J.D., Dalton, J.A., 2000. Experimental comparison of trace element partitioning between clinopyroxene and melt in carbonate and silicate systems and implications for mantle metasomatism. Contrib. Miner. Petrol. 139, 356–371.
Blundy, J.D., Wood, B.J., 1994. Prediction of crystal-melt partition coefficients from elastic moduli. Nature 372, 452–454.
Blundy, J.D., Robinson, J.A.C., Wood, B.J., 1998. Heavy REE are compatible in clinopyroxene on the spinel lherzolite solidus. Earth Planet. Sci. Lett. 160, 493–504.
Blundy, J.D., Wood, B.J., 2003. Partitioning of trace elements between crystals and melts. Earth Planet. Sci. Lett. 210, 383–397.
Bonechi, B., Perinelli, C., Gaeta, M., Fabbrizio, A., Petrelli, M., Strnad, L., 2021. High pressure trace element partitioning between clinopyroxene and alkali basaltic melts. Geochim. Cosmochim. Acta 305, 282–305.
Bonechi, B., Gaeta, M., Perinelli, C., Moschini, P., Romano, C., Vona, A., 2022. Micro-Raman water calibration in ultrapotassic silicate glasses: Application to phonotephrites and K-foidites of Colli Albani Volcanic District (Central Italy). Chem. Geol. 597, 120816.
Brooker, R.A., Du, Z., Blundy, J.D., Kelley, S.P., Allan, N.L., Wood, B.J., Chamorro, E.M., Wartho, J.-A., Purton, J.A., 2003. The "zero charge" partitioning behavior of noble gases during mantle melting. Nature 423, 738–741.
Burns, R.G., 1975. Crystal field effects in chromium and its partitioning in the mantle. In: Chromium: Its Physicochemical Behavior and Petrologic Significance. Pergamon, pp. 857–864.
Condomines, M., Tanguy, J.C., Kieffer, G., Allègre, C.J., 1982. Magmatic evolution of a volcano studied by 230Th-238U disequilibrium and trace elements systematics: The Etna case. Geochim. Cosmochim. Acta 46, 1397–1416.
Corsaro, R.A., Civetta, L., Di Renzo, V., Miraglia, L., 2009. Petrology of lavas from the 2004–2005 flank eruption of Mt. Etna, Italy: inferences on the dynamics of magma in the shallow plumbing system. Bull. Volcanol. 71, 781–793.
Devine, J.D., Gardner, J.E., Brack, H.P., Layne, G.D., Rutherford, M.J., 1995. Comparison of microanalytical methods for estimating H2O contents of silicic volcanic glasses. Am. Mineral. 80, 319–328.
Di Fiore, F., Mollo, S., Vona, A., MacDonald, A., Ubide, T., Nazzari, M., Romano, C., Scarlato, P., 2021. Kinetic partitioning of major and trace cations between clinopyroxene and phonotephritic melt under convective stirring conditions: New insights into clinopyroxene sector zoning and concentric zoning. Chem. Geol. 584, 120531.
Di Genova, D., Sicola, S., Romano, C., Vona, A., Fanara, S., Spina, L., 2017. Effect of iron and nanolites on Raman spectra of volcanic glasses: A reassessment of existing strategies to estimate the water content. Chem. Geol. 475, 76–86.

Di Genova, D., Zandona, A., Deubener, J., 2020. Unravelling the effect of nano-heterogeneity on the viscosity of silicate melts: Implications for glass manufacturing and volcanic eruptions. J. Non Cryst. Solids 545, 120248.
Di Stefano, F., Mollo, S., Ubide, T., Petrone, C.M., Caulfield, J., Scarlato, P., Nazzari, M., Andronico, D., Del Bello, E., 2020. Mush cannibalism and disruption recorded by clinopyroxene phenocrysts at Stromboli volcano: New insights from recent 2003–2017 activity. Lithos 360–361, 105440.
Downes, M.J., 1974. Sector and oscillatory zoning in calcic augites from M. Etna. Sicily. Contrib. Mineral. Petrol. 47, 187–196.
Dowty, E., 1976. Crystal structure and crystal growth: II. Sector zoning in minerals. Am. Mineral. 61, 460–469.
Dowty, E., 1977. The importance of adsorption in igneous partitioning of trace elements. Geochim. Cosmochim. Acta 41, 1643–1646.
Duan, X., 2014. A general model for predicting the solubility behavior of H2O-CO2 fluids in silicate melts over a wide range of pressure, temperature and compositions. Geochim. Cosmochim. Acta 125, 582–609.
Duncan, A.M., Preston, R.M.F., 1980. Chemical variation of clinopyroxene phenocrysts from the trachybasaltic lavas of Mount Etna, Sicily. Min. Mag. 43, 765–770.
Dygert, N., Liang, Y., Sun, C., Hess, P., 2014. An experimental study of trace element partitioning between augite and Fe-rich basalts. Geochim. Cosmochim. Acta 132, 170–186.
Ferguson, A.K., 1973. On hour-glass sector zoning in clinopyroxene. Min. Mag. 39, 321–325.
Forsythe, L.M., Nielsen, R.L., Fisk, M.R., 1994. High-field strength element partitioning between pyroxene and basaltic to dacitic magmas. Chem. Geol. 117, 107–125.
Francis, D., Minarik, W., 2008. Aluminum-dependent trace element partitioning in clinopyroxene. Contrib. Miner. Petrol. 156, 439–451.
Gaetani, G.A., 2004. The influence of melt structure on trace element partitioning near the peridotite solidus. Contrib. Miner. Petrol. 147, 511–527.
Ganguly, J., Saxena, S.K., 1987. Exchange equilibrium and intercrystalline fractionation. In: Mixtures and Mineral Reactions. Mixtures and Mineral Reactions. Springer-Verlag, New York, pp. 131–165.
Giacomoni, P.P., Coltorti, M., Mollo, S., Ferlito, C., Braiato, M., Scarlato, P., 2018. The 2011–2012 paroxysmal eruptions at Mt. Etna volcano: Insights on the vertically zoned plumbing system. J. Volcanol. Geoth. Res. 349, 370–391.
Giuffrida, M., Viccaro, M., 2017. Three years (2011–2013) of eruptive activity at Mt. Etna: working modes and timescales of the modern volcano plumbing system from micro-analytical studies of crystals. Earth Sci. Rev. 171, 289–322.
Green, T.H., Pearson, N.J., 1985. Rare earth element partitioning between clinopyroxene and silicate liquid at moderate to high pressure. Contrib. Miner. Petrol. 91, 24–36.
Gualda, G.A., Ghiorso, M.S., Lemons, R.V., Carley, T.L., 2012. Rhyolite-MELTS: a modified calibration of MELTS optimized for silica-rich, fluid-bearing magmatic systems. J. Petrol. 53, 875–890.
Hart, S.R., Dunn, T., 1993. Experimental cpx-melt partitioning of 24 trace elements. Contrib. Miner. Petrol. 113, 1–8.
Hill, E., Wood, B.J., Blundy, J.D., 2000. The effect of Ca-Tschermaks component on trace element partitioning between clinopyroxene and silicate melt. Lithos 53, 203–215.
Hill, E., Blundy, J.D., Wood, B.J., 2011. Clinopyroxene-melt trace element partitioning and the development of a predictive model for HFSE and Sc. Contrib. Miner. Petrol. 161, 423–438.
Hollister, L.S., Gancarz, A.J., 1971. Compositional sector-zoning in clinopyroxene from the Narce area, Italy. Am. Mineral. 56, 959–979.
Huang, F., Lundstrom, C.C., McDonough, W.F., 2006. Effect of melt structure on trace element partitioning between clinopyroxene and silicic, alkaline, aluminous melts. Am. Mineral. 91, 1385–1400.
Jahn, H.A., Teller, E., 1937. Stability of polyatomic molecules in degenerate electronic states. I. Orbital degeneracy. Proc. R. Soc. A 161, 220–235.
Joron, J.L., Treuil, M., 1984. Étude géochimique et pétrogenèse des laves de l'Etna, Sicile, Italie. Bull. Volcanol. 47, 1125–1144.
Kahl, M., Chakraborty, S., Costa, F., Pompilio, M., 2011. Dynamic plumbing system beneath volcanoes by kinetic modeling, and the connection to monitoring data: an example from Mt. Etna. Earth Planet. Sci. Lett. 308, 11–22.
Kamenetsky, V., Clocchiatti, R., 1996. Primitive magmatism of Mt. Etna: insights from mineralogy and melt inclusions. Earth Planet. Sci. Lett. 142, 553–572.
Kennedy, A.K., Lofgren, G.E., Wasserburg, G.J., 1993. An experimental study of trace-element partitioning between olivine, orthopyroxene and melt in chondrules-equilibrium values and kinetic effects. Earth Planet. Sci. Lett. 115, 177–195.
Kirkpatrick, R.J., 1975. Crystal Growth from the Melt: A Review. Am. Mineral. 60, 798–814.
Kirkpatrick, R.J., 1981. Kinetics of crystallization of igneous rocks. In: Lasaga, A.C., Kirkpatrick, R.J. (Eds.). Rev Mineral Geochem 8, 321–397.
Klemme, S., Blundy, J.D., Wood, B.J., 2002. Experimental constraints on major and trace element partitioning during partial melting of eclogite. Geochim Comsochim Acta 66, 3109–3123.
Kouchi, A., Sugawara, Y., Kashima, K., Sunagawa, I., 1983. Laboratory growth of sector zoned clinopyroxenes in the system $CaMgSi_2O_6$-$CaTiAl_2O_6$. Contr. Mineral. Petrol. 83, 177–184.
Lang, S., Mollo, S., France, L., Misiti, V., Nazzari, M., 2021. Kinetic partitioning of major-minor cations between olivine and Hawaiian tholeiitic basalt under variable undercooling and cooling rate conditions. Chem. Geol. 584, 120485.
Lang, S., Mollo, S., France, L., Misiti, V., Nazzari, M., 2022. Partitioning of Ti, Al, P, and Cr between olivine and a tholeiitic basaltic melt: Insights on olivine zoning patterns and cation substitution reactions under variable cooling rate conditions. Chem. Geol. 601, 120870.
Langer, K., Andrut, M., 1996. The crystal field concept (CFC) in geosciences: Does the crystal field stabilization energy of Cr3+ rule its intercrystalline partitioning behavior?. In: Mineral Spectroscopy: A Tribute to Roger G. Burns, 5. The Geochemical Society, Special Publication, pp. 29–39.
Lasaga, A.C., 1997. Kinetic Theory in the Earth Sciences. Princeton University Press, Princeton, New Jersey, p. 811.
Leung, I.S., 1974. Sector-Zoned titanaugites: morphology, crystal chemistry and growth. Am. Mineral. 59, 127–138.
Lindstrom, D.J., 1976. Experimental study of the partitioning of the transition metals between clinopyroxene and coexisting silicate liquids. PhD Thesis. University of Oregon, OR, USA.
Lofgren, G.E., Huss, G.R., Wasserburg, G.J., 2006. An experimental study of trace-element partitioning between Ti-Al-clinopyroxene and melt: Equilibrium and kinetic effects including sector zoning. Am. Mineral. 91, 1596–1606.
Lundstrom, C.C., Shaw, H.F., Ryerson, F.J., Phinney, D.L., Gill, J.B., Williams, Q., 1994. Compositional controls on the partitioning of U, Th, Ba, Pb, Sr and Zr between clinopyroxene and haplobasaltic melts: implications for uranium series disequilibria in basalts. Earth Planet. Sci. Lett. 128, 407–423.
Lundstrom, C.C., Shaw, H.F., Ryerson, F.J., Williams, Q., Gill, J., 1998. Crystal chemical control of clinopyroxene-melt partitioning in the Di–Ab–An system: implications for elemental fractionations in the depleted mantle. Geochim. Cosmochim. Acta 62, 2849–2862.
MacDonald, A., Ubide, T., Mollo, S., Masotta, M., Pontesilli, A., 2022. Trace element partitioning in zoned clinopyroxene as a proxy for undercooling: Experimental constraints from trachybasaltic magmas. Geochim. Cosmochim. Acta 336, 249–268.
Mallmann, G., O'Neill, H.S.C., 2009. The crystal/melt partitioning of V during mantle melting as a function of oxygen fugacity compared with some other elements (Al, P, Ca, Sc, Ti, Cr, Fe, Ga, Y, Zr and Nb). J. Petrol. 50, 1765–1794.
Marks, M., Halama, R., Wenzel, T., Markl, G., 2004. Trace element variations in clinopyroxene and amphibole from alkaline to peralkaline syenites and granites: Implications for mineral-melt trace-element partitioning. Chem. Geol. 211, 185–215.
Masotta, M., Pontesilli, A., Mollo, S., Armienti, P., Ubide, T., Nazzari, M., Scarlato, P., 2020. The role of undercooling during clinopyroxene growth in trachybasaltic magmas: Insights on magma decompression and cooling at Mt. Etna volcano. Geochim. Cosmochim. Acta 268, 258–276.
McKay, G., Le, L., Wagstaff, J., Crozaz, G., 1994. Experimental partitioning of rare earth elements and strontium: Constraints on petrogenesis and redox conditions during crystallization of Antarctic angrite Lewis Cliff 86010. Geochim. Cosmochim. Acta 58, 2911–2919.
Miyajima, N., Fujino, K., Funamori, N., Kondo, T., Yagi, T., 1999. Garnet-perovskite transformation under the Earth's lower mantle conditions: An analytical transmission electron microscopy study. Phys. Earth Planetary Interior 116, 117–131.
Mollo, S., Hammer, J.E., 2017. Dynamic crystallization in magmas. EMU Notes Mineral. 16, 373–418.
Mollo, S., Del Gaudio, P., Ventura, G., Iezzi, G., Scarlato, P., 2010. Dependence of clinopyroxene composition on cooling rate in basaltic magmas: Implications for thermobarometry. Lithos 118, 302–312.
Mollo, S., Misiti, V., Scarlato, P., Soligo, M., 2012. The role of cooling rate in the origin of high temperature phases at the chilled margin of magmatic intrusions. Chem. Geol. 322–323, 28–46.
Mollo, S., Blundy, J.D., Iezzi, G., Scarlato, P., Langone, A., 2013. The partitioning of trace elements between clinopyroxene and trachybasaltic melt during rapid cooling and crystal growth. Contrib. Miner. Petrol. 166, 1633–1654.
Mollo, S., Giacomoni, P.P., Coltorti, M., Ferlito, C., Iezzi, G., Scarlato, P., 2015. Reconstruction of magmatic variables governing recent Etnean eruptions: Constraints from mineral chemistry and P-T–fO_2–H_2O modeling. Lithos 212–215, 311–320.
Mollo, S., Forni, F., Bachmann, O., Blundy, J.D., De Astis, G., Scarlato, P., 2016. Trace element partitioning between clinopyroxene and trachy-phonolitic melts: A case study from the Campanian Ignimbrite (Campi Flegrei, Italy). Lithos 252–253, 160–172.
Mollo, S., Vetere, F., Beherens, H., Tecchiato, V., Langone, A., Scarlato, P., Perugini, D., 2017. The effect of degassing and volatile exsolution on the composition of a trachybasaltic melt decompressed at slow and fast rates. Periodico di Mineralogia 86, 185–197.
Mollo, S., Blundy, J., Scarlato, P., De Cristofaro, S.P., Tecchiato, V., Di Stefano, F., Vetere, F., Holtz, F., Bachmann, O., 2018. An integrated P-T-H_2O-lattice strain model to quantify the role of clinopyroxene fractionation on REE+Y and HFSE patterns of mafic alkaline magmas: Application to eruptions at Mt. Etna. Earth-Sci. Rev. 185, 32–56.
Mollo, S., Ubide, T., Di Stefano, F., Nazzari, M., Scarlato, P., 2020a. Polybaric/polythermal magma transport and trace element partitioning recorded in single crystals: A case study of a zoned clinopyroxene from Mt. Etna. Lithos 356–357, 105382.
Mollo, S., Blundy, J., Scarlato, P., Vetere, F., Holtz, F., Bachmann, O., Gaeta, M., 2020b. A review of the lattice strain and electrostatic effects on trace element partitioning between clinopyroxene and melt: Applications to magmatic systems saturated with Tschermak-rich clinopyroxenes. Earth Sci. Rev. 210, 103351.
Moschini, P., Mollo, S., Gaeta, M., Fanara, S., Nazzari, M., Petrone, C.M., Scarlato, P., 2021. Parameterization of clinopyroxene growth kinetics via crystal size distribution (CSD) analysis: Insights into the temporal scales of magma dynamics at Mt. Etna volcano. Lithos 396–397, 106225.
Moschini, P., Mollo, S., Pontesilli, A., Nazzari, M., Petrone, C.M., Fanara, S., Vona, A., Gaeta, M., Romano, C., Scarlato, P., 2023. A review of plagioclase growth rate and compositional evolution in mafic alkaline magmas: Guidelines for thermometry, hygrometry, and timescales of magma dynamics at Stromboli and Mt. Etna. Earth Sci. Rev. 240, 104399.

Nakamura, Y., 1973. Origin of sector-zoning of igneous clinopyroxenes. Am. Mineral. 58, 986–990.
Nazzari, M., Di Stefano, F., Mollo, S., Scarlato, P., Tecchiato, V., Ellis, B., Bachmann, O., Ferlito, C., 2019. Modeling the crystallization and emplacement conditions of a basaltic trachyandesitic sill at Mt. Etna volcano. Minerals 9, 126.
Nicotra, E., Viccaro, E., Ferlito, C., Cristofolini, R., 2010. Influx of volatiles into shallow reservoirs at Mt. Etna volcano (Italy) responsible for halogen-rich magmas. Eur. J. Mineral. 22, 121–138.
O'Leary, J.A., Gaetani, G.A., Hauri, E.H., 2010. The effect of tetrahedral Al^{3+} on the partitioning of water between clinopyroxene and silicate melt. Earth Planet. Sci. Lett. 297, 111–120.
Onuma, N., Higuchi, H., Wakita, H., Nagasawa, H., 1968. Trace element partition between two pyroxenes and the host lava. Earth Planet. Sci. Lett. 5, 47–51.
Ottonello, G., Della Giusta, A., Dal Negro, A., Baccarin, F., 1992. A structure energy model for C2/c pyroxenes in the system Na-Mg-Ca-Mn-Fe-AI-Cr-Ti-Si-O. In: Saxena, S.K. (Ed.), Advances in Physical Geochemistry, Thermodynamic Data. Springer, New York, Berlin, pp. 194–238.
Paquette, J., Reeder, R.J., 1990. New type of compositional zoning in calcite: Insights into crystal-growth mechanisms. Geology 18, 1244–1247.
Paton, C., Hellstrom, J., Paul, B., Woodhead, J., Hergt, J., 2011. Iolite: freeware for the visualisation and processing of mass spectrometric data. J. Anal. At. Spectrom 26 (12), 2508–2518.
Petrone, C.M., Mollo, S., Gertisser, R., Buret, Y., Scarlato, P., Del Bello, E., Andronico, D., Ellis, B., Pontesilli, A., De Astis, G., Giacomoni, P.P., Coltorti, M., Reagan, M., 2022. Magma recharge and mush rejuvenation drive paroxysmal activity at Stromboli volcano. Nat. Commun. 13.
Petrus, J.A., Chew, D.M., Leybourne, M.I., Kamber, B.S., 2017. A new approach to laser-ablation inductively-coupled-plasma mass spectrometry (LA-ICP-MS) using the flexible map interrogation tool 'Monocle'. Chem. Geol. 463, 76–93.
Pontesilli, A., Masotta, M., Nazzari, M., Mollo, S., Armienti, P., Scarlato, P., Brenna, M., 2019. Crystallization kinetics of clinopyroxene and titanomagnetite growing from a trachybasaltic melt: New insights from isothermal time-series experiments. Chem. Geol. 510, 113–129.
Purton, J.A., Allan, N.L., Blundy, J.D., 1997. Calculated solution energies of heterovalent cations in forsterite and diopside: Implications for trace element partitioning. Geochim. Cosmochim. Acta 61, 3927–3936.
Putirka, K., 2016. Special Collection: Olivine: Rates and styles of planetary cooling on Earth, Moon, Mars, and Vesta, using new models for oxygen fugacity, ferric-ferrous ratios, olivine-liquid Fe-Mg exchange, and mantle potential temperature. Am. Mineral. 101, 819–840.
Qian, Q., Hermann, J., Wang, Y., Guo, J., Liu, F., Wang, L., 2015. Variations of clinopyroxene/melt element partitioning during assimilation of olivine/peridotite by low-Mg diorite magma. Chem. Geol. 419, 36–54.
Ray, G.L., Shimizu, N., Hart, S.R., 1983. An ion microprobe study of the partitioning of trace elements between clinopyroxene and liquid in the system diopside-albite-anorthite. Geochim. Cosmochim. Acta 47, 2131–2140.
Sack, R.O., Ghiorso, M.S., 1994. Thermodynamics of multicomponent pyroxenes: I. Formulation of a general model. Contrib. Miner. Petrol. 116, 277–286.
Scarani, A., Zandonà, A., Di Fiore, F., Valdivia, P., Putra, R., Miyajima, N., Bornhöft, H., Vona, A., Deubener, J., Romano, C., Di Genova, D., 2022. Commun. Earth Environ. 3, 284.
Scarlato, P., Mollo, S., Blundy, J., Iezzi, G., Tiepolo, M., 2014. The role of natural solidification paths on REE partitioning between clinopyroxene and melt. Bull. Volcanol. 76, 810.
Schmidt, M.W., Connolly, J.A.D., Günther, D., Bogaerts, M., 2006. Element partitioning: the role of melt structure and composition. Science 312, 1646–1650.
Schosnig, M., Hoffer, E., 1998. Compositional dependence of REE partitioning between diopside and melt at 1 atmosphere. Contrib. Miner. Petrol. 133, 205–216.
Shannon, R.D., 1976. Revised effective ionic radii and systematic studies of interatomic distances in halides and chalcogenides. Acta Crystallogr. 32, 751–767.
Shannon, R.D., 1993. Dielectric polarizabilities of ions in oxides and fluorides. J. Appl. Phys. 73, 348–366.
Shearer, C.K., McKay, G., Papike, J.J., Karner, J.M., 2006. Pyroxene europium valence oxybarometer: Effects of pyroxene composition, melt composition, and crystallization kinetics. Amer. Min. 91, 1657–1663.
Shimizu, N., 1981. Trace element incorporation into growing augite phenocryst. Nature 289, 575–577.
Simakin, A.G., Salova, T.P., Armienti, P., 2003. Kinetics of clinopyroxene growth from a hydrous hawaiite melt. Geochem. Int. 41, 1275–1286.
Skulski, T., Minarik, W., Watson, E.B., 1994. High pressure experimental trace-element partitioning between clinopyroxene and basaltic melts. Chem. Geol. 117, 127–147.
Stewart, M.L., Pearce, T.H., 2004. Sieve-textured plagioclase in dacitic magma: Interference imaging results. Am. Mineral. 89, 348–351.
Sun, C., Liang, Y., 2012. Distribution of REE between clinopyroxene and basaltic melt along a mantle adiabat: effects of major element composition, water, and temperature. Contrib. Miner. Petrol. 163, 807–823.
Sun, C.G., Liang, Y., 2013. The importance of crystal chemistry on REE partitioning between mantle minerals (garnet, clinopyroxene, orthopyroxene, and olivine) and basaltic melts. Chem. Geol. 358, 23–36.
Sunagawa, I., 2005. Crystals: Growth, Morphology and Perfection. Cambridge University Press, Cambridge.
Tanguy, J.C., 1978. Tholeiitic basalt magmatism of Mount Etna and its relations with the alkaline series. Contrib. Miner. Petrol. 66, 51–67.
Tanguy, J.C., Condomines, M., Kieffer, G., 1997. Evolution of Mount Etna magma: constraint on the present feeding system and eruptive mechanism. J. Volcanol. Geoth. Res. 75, 221–250.
Toplis, M.J., Corgne, A., 2002. An experimental study of element partitioning between magnetite, clinopyroxene and iron-bearing silicate liquids with particular emphasis on vanadium. Contrib. Miner. Petrol. 144, 22–37.
Tsuchiyama, A., 1985. Crystallization kinetics in the system CaMgSi206-$CaAl_2Si_2O_8$: development of zoning and kinetics effects on element partitioning. Am. Mineral. 70, 474–486.
Ubide, T., Kamber, B.S., 2018. Volcanic crystals as time capsules of eruption history. Nat. Commun. 9.
Ubide, T., McKenna, C.A., Chew, D.M., Kamber, B.S.K., 2015. High-resolution LA-ICP-MS trace element mapping of igneous minerals: in search of magma histories. Chem. Geol. 409, 157–168.
Ubide, T., Mollo, S., Zhao, J., Nazzari, M., Scarlato, P., 2019a. Sector-zoned clinopyroxene as a recorder of magma history, eruption triggers, and ascent rates. Geochim. Cosmochim. Acta 251, 265–283.
Ubide, T., Caulfield, J., Brandt, C., Bussweiler, Y., Mollo, S., Di Stefano, F., Nazzari, M., Scarlato, P., 2019b. Deep magma storage revealed by multi-method elemental mapping of clinopyroxene megacrysts at Stromboli volcano. Front. Earth Sci. 7, 239.
Van Cappellen, E., 1990. The parameterless correction method in X-ray microanalysis. Microsc. Microstruct. Microanal. 1, 1–22.
Van Cappellen, E., Doukhan, J.C., 1994. Quantitative transmission X-ray microanalysis of ionic compounds. Ultramicroscopy 53, 343–349.
Viccaro, M., Calcagno, R., Garozzo, I., Giuffrida, M., Nicotra, E., 2015. Continuous magma recharge at Mt. Etna during the 2011–2013 period controls the style of volcanic activity and compositions of erupted lavas. Mineral. Petrol. 109, 67–83.
Watson, E.B., Liang, Y., 1995. A simple model for sector zoning in slowly grown crystals: implications for growth rate and lattice diffusion, with emphasis on accessory minerals in crustal rocks. Am. Mineral. 80, 1179–1187.
Watson, E.B., Müller, T., 2009. Non-equilibrium isotopic and elemental fractionation during diffusion-controlled crystal growth under static and dynamic conditions. Chem. Geol. 267, 111–124.
White, W.M., 2013. Geochemistry. Wiley-Blackwell, 960 pages. ISBN: 978-1-119-43805-2.
Wood, B.J., 1976. Mixing properties of tschermakitic clinopyroxenes. Am. Mineral. 61, 599–602.
Wood, B.J., 1979. Activity-composition relationships in Ca(Mg, Fe)Si2O6-CaAl2SiO6 clinopyroxene solid-solutions. Am. J. Sci. 279, 854–875.
Wood, B.J., Blundy, J.D., 1997. A predictive model for rare earth element partitioning between clinopyroxene and anhydrous silicate melt. Contrib. Miner. Petrol. 129, 166–181.
Wood, B.J., Blundy, J.D., 2001. The effect of cation charge on crystal–melt partitioning of trace elements. Earth Planet. Sci. Lett. 188, 59–71.
Wood, B.J., Blundy, J.D., 2014. Trace Element Partitioning: The Influences of Ionic Radius, Cation Charge, Pressure, and Temperature. Treatise on Geochemistry, second ed. Elsevier, Oxford, pp. 421–448.
Wood, B.J., Trigila, R., 2001. Experimental determination of aluminous clinopyroxene-melt partition coefficients for potassic liquids, with application to the evolution of the Roman province potassic magmas. Chem. Geol. 172, 213–223.
Yao, L.J., Sun, C.G., Liang, Y., 2012. A parameterized model for REE distribution between low-ca pyroxene and basaltic melts with applications to REE partitioning in low-ca pyroxene along a mantle adiabat and during pyroxenite-derived melt and peridotite interaction. Contrib. Miner. Petrol. 164, 261–280.
Zhang, Y., 2010. Diffusion in minerals and melts: theoretical background. In: Zhang, Y., Cherniak, D. (Eds.), Diffusion in Minerals and Melts. Rev. Mineral. Geochem., 72, pp. 5–60.
Zhang, L., Guo, X., Wang, Q., Ding, J., Ni, H., 2017. Diffusion of hydrous species in model basaltic melt. Geochim. Cosmochim. Acta 215, 377–386.